

## Article

# In Situ Geochemical Evaluation of Retrograde Hydration Effects in the Peri-Siberian Forearc Mantle (Khara-Nur and Alag-Khadny Peridotite Complexes)

Anas A. Karimov <sup>1,2</sup>, Marina A. Gornova <sup>1</sup>, Vasiliy A. Belyaev <sup>1</sup>, Sergei Yu. Skuzovatov <sup>1,\*</sup>, Alexander Ya. Medvedev <sup>1</sup> and Nikolay V. Bryanskiy <sup>2,3</sup>

<sup>1</sup> Vinogradov Institute of Geochemistry, Russian Academy of Sciences, Siberian Branch, 1A Favorovskogo Str., 664033 Irkutsk, Russia; anas@igc.irk.ru (A.A.K.); mgorn@igc.irk.ru (M.A.G.); belyaev@igc.irk.ru (V.A.B.); amedv@igc.irk.ru (A.Y.M.)

<sup>2</sup> Institute of the Earth's Crust, Russian Academy of Sciences, Siberian Branch, 128 Lermontova Str., 664033 Irkutsk, Russia; tridigron@yandex.ru

<sup>3</sup> Physical Department, Irkutsk State University, 20 Gagarina Blvd., 664002 Irkutsk, Russia

\* Correspondence: skuzovatov@igc.irk.ru

**Abstract:** In order to assess the geochemical effects of retrograde metamorphic rehydration, fluid metasomatism, and the fluid-mobile elements (FMEs) budget in the case of oceanic and continental subduction, we report the petrography, bulk, and in situ LA-ICP-MS trace-element data for the two poorly studied ophiolites in the northern (Khara-Nur, Eastern Sayan, Russia) and central (Alag-Khadny accretionary wedge, SW Mongolia) parts of the peri-Siberian orogenic framing. Both complexes are relics of the ancient oceanic mantle, which was subjected to processes of partial melting, metasomatism, and retrograde metamorphism. Typical mineral assemblages include olivine + orthopyroxene + chlorite + tremolite ± secondary olivine (640–800 °C), olivine + antigorite ± secondary clinopyroxene (<640 °C), and olivine + chrysotile ± secondary clinopyroxene (<250 °C) and are stable at pressures up to 2 GPa. Hydration and partial serpentinization of mantle peridotites lead to tremolite formation after orthopyroxene, followed by olivine replacement by antigorite. Serpentine-group minerals (antigorite and chrysotile) were distinguished by Raman spectroscopy, and the contents of incompatible elements (mobile and immobile in fluids) in metamorphic minerals (tremolite, antigorite, and chrysotile) were examined in situ by LA-ICP-MS. The behavior of conservative HFSE (Zr, Nb, Ta, and Ti) and—in part—HREE does not distinguish between the two types (oceanic and continental) of subduction environments. Different patterns of FMEs (Cs, Rb, Ba, U, Sb, Pb, Sr, and LREE) enrichment in metaperidotites reflect variations in the slab fluid composition, which was primarily governed by the contrasting nature of subducted lithologies. The affinity of Alag-Khadny to the subduction of a continental margin is recorded by increased FME contents and selective enrichment by some moderately mobile elements, such as U, Th, and LREE, with respect to the oceanic-type subduction environment of Khara-Nur. Distinct patterns of FME enrichment in tremolite and antigorite from two complexes indicate different sequences of fluid-induced replacement, which was controlled by Opx composition. We demonstrate that evaluation of the initial composition of precursor minerals affected by multi-stage melting and melt metasomatism should be considered with care to estimate the differential fluid overprint and associated elemental uptake from subduction fluids.

**Keywords:** Central Asian Orogenic Belt; subduction zones; ophiolites; metaperidotites; serpentinites; fluid metasomatism



**Citation:** Karimov, A.A.; Gornova, M.A.; Belyaev, V.A.; Skuzovatov, S.Y.; Medvedev, A.Y.; Bryanskiy, N.V. In Situ Geochemical Evaluation of Retrograde Hydration Effects in the Peri-Siberian Forearc Mantle (Khara-Nur and Alag-Khadny Peridotite Complexes). *Minerals* **2024**, *14*, 457. <https://doi.org/10.3390/min14050457>

Academic Editor: Basilios Tsikouras

Received: 29 March 2024

Revised: 22 April 2024

Accepted: 23 April 2024

Published: 26 April 2024



**Copyright:** © 2024 by the authors. Licensee MDPI, Basel, Switzerland. This article is an open access article distributed under the terms and conditions of the Creative Commons Attribution (CC BY) license (<https://creativecommons.org/licenses/by/4.0/>).

## 1. Introduction

Subduction zones are major sites of crustal recycling and mantle–crust interaction. The onset of subduction disrupts the thermal and geochemical equilibrium of rocks in the upper mantle and leads to low-temperature–high-pressure (LT–HP) metamorphism, fluid

and melt metasomatism, and magmatism at crust–mantle boundaries. The recycling of crustal rocks and sediments is now accepted as the primary reason for the geochemical heterogeneity of the mantle [1–4], whereas fluid transfer between the subducted lithosphere and the suprasubduction mantle governs most of the subduction-zone cycling of volatiles and fluid-mobile elements (FMEs). Thus, studies on fluid–rock interaction processes at slab–mantle interfaces and within the mantle wedge provide vital information for understanding the compositional evolution of the upper mantle [4–7].

Recent studies have emphasized the major role of hydrous minerals in recording the fluid–peridotite interaction, as they may act as in situ reservoirs of volatiles and FMEs [4,8–13]. The generation of secondary hydrous minerals in mantle-wedge peridotites is a hydrothermal process, whereby there is an interaction between primary peridotite silicates (olivine and pyroxenes) and hydrous fluids [10]. Hydrous minerals (mainly amphibole, chlorite, and serpentine) may incorporate up to 20 wt.% H<sub>2</sub>O and are stable to depths of ~150 km, making them an excellent reservoir for FMEs in supra-subduction environments [9,11,14–16]. Normally, FME (re-)distribution depends on a number of parameters, including the mineralogical composition of the protolith [17]; the depth (and hence, pressure) of the serpentinization process [18]; the lithology of subducted rocks, the subduction regime, and the type of subduction [4,11,19]. In particular, chrysotile and lizardite form at low-temperature conditions below 300 °C, whereas antigorite and tremolite are formed and may be stable at a wide temperature range of 300–650 °C and 600–800 °C, respectively [20–25], that affects both their FME capacity and the composition of released fluids from serpentine-group mineral dehydration breakdown. The in situ studies of hydrous minerals thus make it possible to estimate the budget of FME introduction into the slab–mantle interface relative to the recorded former processes of melting and melt metasomatism and deepen our understanding of FME migration within the mantle wedge and subduction-zone factory.

Three domains of variably hydrated peridotites co-exist in subduction zone sections, including (1) abyssal peridotites variably hydrated by seawater along deep faults ([8,9,26] and refs therein), (2) serpentinites of the subduction channel at the contact between a slab and mantle wedge ([10,18,27,28] and refs therein), and (3) mantle-wedge metaperidotites located on top of the abovementioned domains [29–34]. Metaperidotites of the subducted slab are characterized by prograde replacement of low-temperature hydrous assemblages by higher-T and anhydrous metamorphic phases due to a gradual increase in temperature and pressure. Mantle-wedge metaperidotites exhibit a reversed (retrograde) path of metamorphic transformation, with the replacement of primary anhydrous minerals by high-T and, further, by lower-T hydrous assemblages. Most studies have focused on the first two, while studies on mantle-wedge metaperidotites have yet been limited to fragmentary data on the whole-rock composition and major elements in mineral phases [29–34]. Among the latter, the behavior of FMEs in metamorphic minerals in serpentinites and metaperidotites was investigated mainly in abundant oceanic-type subduction ophiolites [18,35]. The subduction of continental rocks (i.e., granitoids and acid volcanics, sediments, and carbonate rocks), which are geochemically distinct and may be significantly drier with respect to the oceanic lithosphere, may lead to different dehydration conditions and volumes of fluid generation, and produce distinct patterns of fluid enrichment, as, for instance, reported by [9,11]. Here, we report the petrography, bulk, and in situ LA-ICP-MS trace-element data for the two poorly studied ophiolites in the northern (Khara-Nur, Eastern Sayan, Russia) and central (Alag-Khadny accretionary wedge, SW Mongolia) parts of the peri-Siberian orogenic framing to assess and compare the potential geochemical effects of metamorphic rehydration, fluid metasomatism, and the FME budget in the case of oceanic and continental subduction.

## 2. Geological Setting and Sample Petrography

The Central Asian Orogenic Belt (CAOB) is one of the world's largest accretionary orogens that formed due to the closure of the Paleo-Asian Ocean in the Neoproterozoic–Paleozoic and the subsequent collision of the Siberian, Tarim, and North China cratons [36,37]. The formation of the CAOB began with the Neoproterozoic accretion of intraoceanic island arcs to the southern and southwestern margins of the Siberian craton (Figure 1A,B) [37,38]. Further, during the rest of the Paleozoic, many island-arc (continental and oceanic types) terranes and microcontinents continued to accrete to the southern and western margins of the Siberian craton [37,39–41]. As a result, suprasubduction ophiolites of Mesoproterozoic to Paleozoic ages are juxtaposed in the present CAOB collage.

### 2.1. Khara-Nur Metaperidotites

The Khara-Nur (KN) ultramafic massif is located within the Tuva-Mongolian microcontinent in the southeastern part of the Eastern Sayan mountain range. The area has a thrust-sheet structure [42], in which the autochthonous rocks of the Early Precambrian crystalline basement (Gargan Block) are covered by Proterozoic rocks of the Irkut and Ilchir Formations. The Irkut Formation is composed predominantly of limestones and dolomites, and the Ilchir Formation is composed of black shales and mafic metavolcanics, while both are overlain by an ophiolitic cover. The latter contains fragments of residual mantle peridotites (Ilchir Complex), ultramafic-mafic cumulates (Bokson and Zhokhoy Complexes), and a complex of parallel dykes and volcanics (Ospin and Dunzhugur Formations) [42]. The lava and dyke complex chemically resemble the rocks of boninite and island-arc tholeiite series [43]. The presence of boninites is attributed to the Eastern Sayan ophiolites to suprasubduction ophiolites associated with Mariana-type subduction [44,45] and also indicates their proximity to forearc ophiolites, which are quite widespread within CAOB [37,46,47]. The regional metamorphism of the Irkut, Ilchir and Ospin formations corresponds to the conditions of greenschist facies [42].

The KN massif extends for ~25 km from the Urik River in the northeastern direction with a width of 1–7 km (Figure 1B). It overlies the rocks of the Gargan Block at its northwestern boundary. Ultramafics of the massif are part of the ophiolitic cover, which tectonically combines intrusive rocks (gabbroids and pyroxenites of the Bokson Complex) and volcanics (Ospin Formation) [42]. The ophiolite cover is underlain by sediments of the Irkut and Ilchir Formations. In the northwest, it has a tectonic contact with phosphate-bearing carbonate strata of the Bokson Series (Figure 1B). The massif is mainly composed of serpentinized dunites and harzburgites; serpentinites and talc-carbonate rocks are located in the western part of the massif and along its southern and northern margins (Figure 1B) [48]. Olivine-antigorite-diopside (Ol-Atg-Di), olivine-tremolite (Ol-Tr), and olivine-orthopyroxene-tremolite (Ol-Opx-Tr) metaperidotites are developed alternately on the northwestern slope of the Ulan-Khoda mountain, and harzburgites are found closer to the top (Figure 1C). Transitions between all varieties of rocks are not sharp but gradual. According to recent studies [46,47], primary harzburgites and dunites of Khara-Nur represent relics of the ancient subcontinental lithospheric mantle involved in a subduction zone within the Paleoasian Ocean.

Metaperidotites are found in most parts of the Khara-Nur massif. Ol-Atg-Di and Ol-Tr metaperidotites are dark green and black rocks with massive structures and porphyroblastic textures and are composed predominantly of serpentine, which is represented by thin radiating cross-bedded fibers, with relics of primary olivine (Figure 2C). Secondary Di and Tr are also present, which replace primary Opx (Figure 2E–I). Ol-Opx-Tr metaperidotites are fine-grained rocks of dark green and black color with granoblastic-lepidoblastic massive structures. Spinel is present as large (up to 1 mm) irregular-shaped grains, often with magnetite rims of variable thickness from the first  $\mu\text{m}$  to ~100  $\mu\text{m}$  (Figure 2A,B). The amount of primary Ol varies from 40 to 70 vol.% at a size from first tens to first hundreds of microns (Figure 2A–D). Olivine relics often form intergrowths with a fibrous mixture of two serpentines (Atg and Ctl) (Figure 2A), antigorite alone (Figure 2B,C), or chrysotile alone

(Figure 2D). Opx is present as large elongated porphyroclasts up to 2 mm. (Figure 2E–G) and is replaced by Tr along margins and fractures (Figure 2E–G). Opx is often completely replaced by a mixture of tremolite and secondary Ol together with Atg ± Ctl (Figure 2H,I). Primary Cpx is almost absent in metaperidotites and was presumably replaced by tremolite, whereas the first vol.% of Cpx is present in unaltered harzburgites [44].

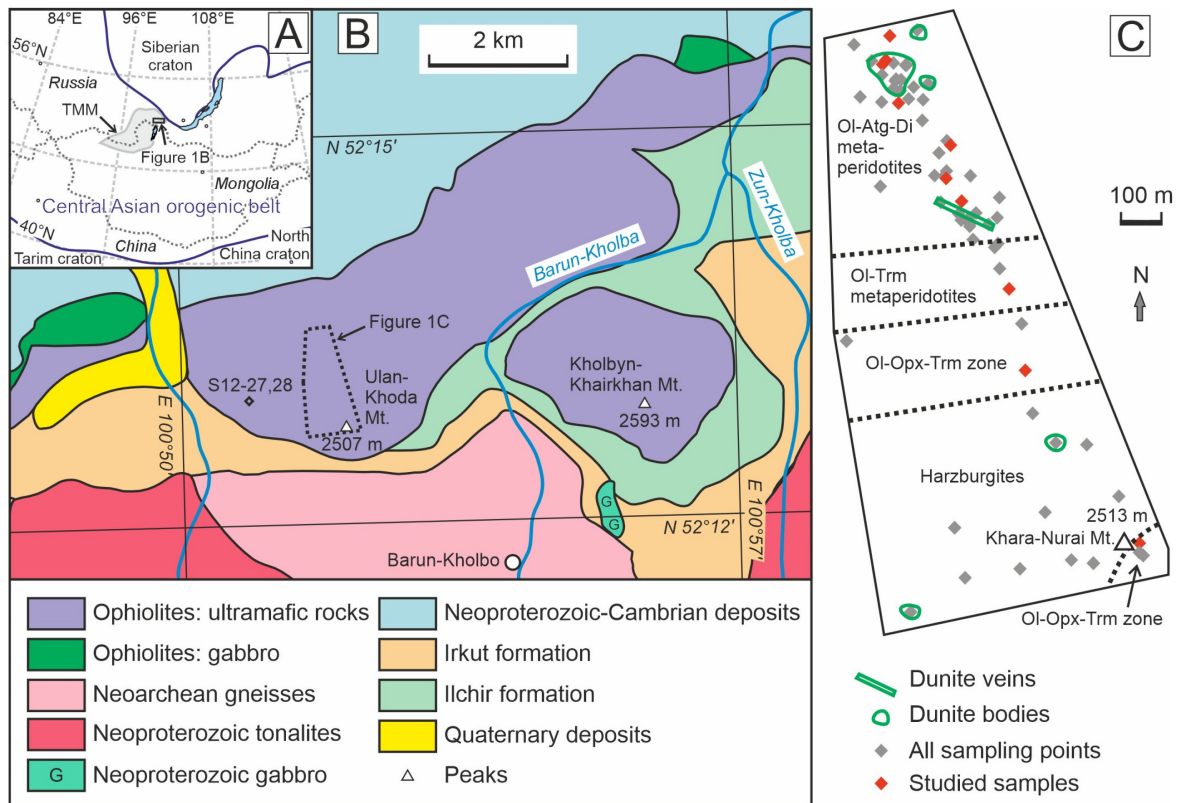


**Figure 1.** Simplified geological scheme of the Khara-Nur massif and its structural position in the Central Asian Orogenic Belt (CAOB). (A) General structure of the CAOB and surrounding cratons [49,50] with TMM contour. (B) Detailed geologic map of the Khara-Nur massif and adjacent areas with additions [42,51]. (C) Geological scheme of the detailed area study with the location of primary harzburgites and metaperidotites and their metamorphic counterparts sampled [47].

Secondary minerals, including serpentine (antigorite and chrysotile), Tr, secondary Ol, and Di, are developed after primary parageneses of KN peridotites. Serpentine is presented in two generations, including high-temperature (250–550 °C) Atg and low-temperature (<250 °C) chrysotile. Atg forms thin flakes, which are mainly located along the margins and fractures of primary Ol (Figure 2B,C) and near Opx (Figure 2F). Atg is often found mixed with Ctl and developed on both Ol (Figure 2A) and orthopyroxene (Figure 2E,H). Ctl forms shapeless tangled fibrous aggregates, which develop after both primary Ol along margins and fractures (Figure 2D; Figure S1A,B in Supplementary File S1) and may partially replace Atg (Figure 2E,H). There is also petrographic evidence of Ctl growth on Atg, which supports the later-stage formation of Ctl (Figure S1C in Supplementary File S1). Serpentinization of primary Ol may produce magnetite (Figure 2C). Tr replaces only Opx along its margins and fractures (Figure 2E–G) and is sometimes observed together with secondary Ol (Figure 2I). It forms clusters of small-sized elongated needle-like crystals. Secondary Ol occurs only in association with Tr (Figure 2H,I), where it is further replaced by secondary Di (Figure 2F,G).

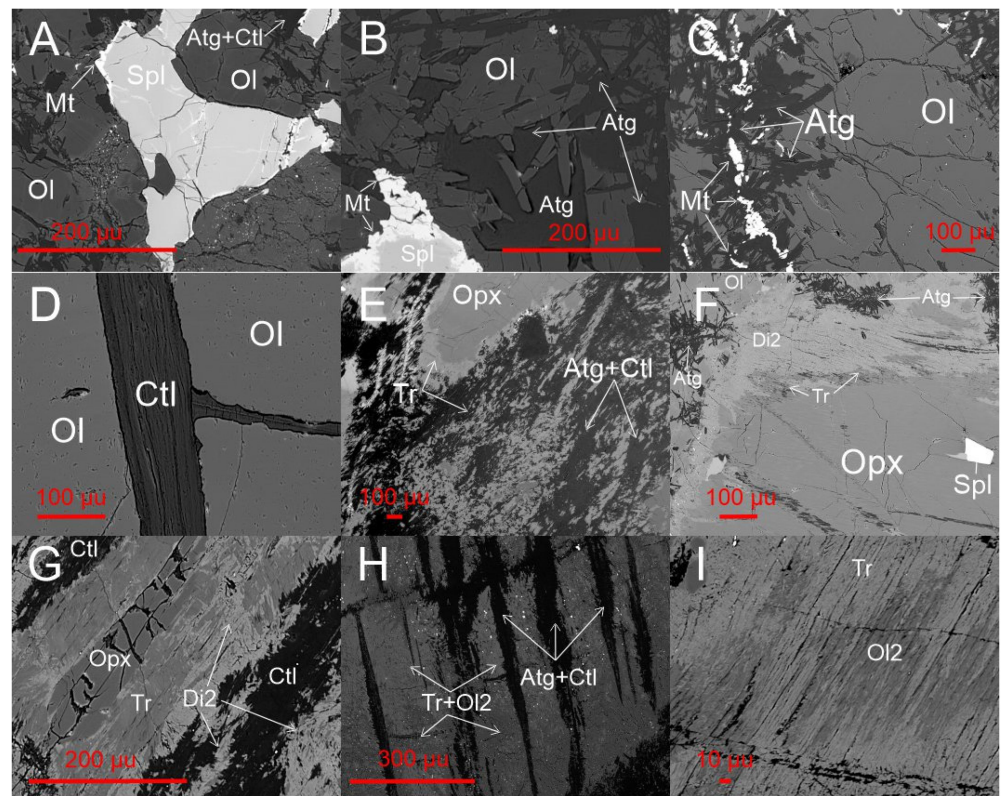


**Figure 2.** Petrographic features of metaperidotites of the Khara-Nur massif (BSE photomicrographs). (A) Development of thin magnetite (Mt) rim around Cr-spinel (Spl) and the beginning of serpentinization process of olivine (Ol) after antigorite (Atg) and chrysotile (Ctl), S21-86. (B) Replacement of Cr-spinel by magnetite and development of antigorite after olivine, S21-102. (C) Replacement of olivine by antigorite with formation of magnetite, S18-121. (D) Replacement of primary olivine by chrysotile, S18-12. (E) Relic of orthopyroxene (Opx) and development of tremolite (Tr) after Opx, tangled fibrous aggregates of antigorite and chrysotile of the rock matrix, S18-15. (F) Relics of a large orthopyroxene porphyroblast and a smaller olivine grain, with tremolite (after Opx) and antigorite (after Ol) in between, as well as secondary diopside (Di2) after tremolite, S21-92. (G) A relic of orthopyroxene with tremolite and secondary diopside after Opx; note an aggregate of fibrous chrysotile, S21-86. (H) The occurrence of bastite after orthopyroxene, which consists of equilibrium mixture of antigorite, chrysotile, and tremolite with secondary olivine (Ol2), S21-85. (I) An enlarged area of orthopyroxene replacement by tremolite and secondary olivine, S18-128.

## 2.2. Alag-Khadny Metaperidotites

The Alag-Khadny (AK) accretionary complex (or accretionary wedge) is located in the western part of the Gobi-Altay zone near the intersection of the Main Mongolian Lineament and the suture zone between the Dzabkhan-Baidrag microcontinent [52] and the Lake Zone. The latter includes a number of the Early Paleozoic ophiolites and subduction-accretionary complexes ([53,54] and refs therein). Within the AK, basement granite-gneiss rocks of the Zamtyin-Nuru crystalline complex (~950 Ma; [54,55]) are associated with metasedimentary rocks, including metapelites found at the southern margin of AK, which might represent a sedimentary cover of an Early Neoproterozoic rifted continental margin [55]. The whole AK structure is tectonically overlain by volcanogenic-sedimentary and carbonate rocks of the Tsakhir-Uul Formation with Early Cambrian fauna [56]. Eclogites were reported in AK as individual boudins (up to several hundred meters) in metasedimentary rocks and carbonates and are spatially associated with the spread of orthogneisses and metapelites [39,40]. Based on geochemical characteristics similar to the T-MORB basalts, high-pressure rocks were originally attributed to an accretionary complex of Early Cambrian subduction [57]. More recent models suggest the formation of sedimentary and igneous rock protoliths in a

continental-margin setting that evolved from Early Neoproterozoic rifting [40] or supra-subduction back-arc magmatism [54] to the Early Caledonian subduction-accretionary stage (540–530 Ma). The eclogite-facies metamorphism (600–620 °C, 1.9–2.1 GPa) is interpreted as the result of subduction of the continental margin [37,52], when predominantly felsic (metagranitoid and metasedimentary) rock with a subordinate amount of mafic crust was buried beneath the oceanic crust [55]. From the south, the high-pressure AK rocks are in tectonic contact with pre-Early Cambrian carbonates of the Maikhan-Tsakhir Formation, which hosts bodies of low- to medium-pressure mafic amphibolites. The latter were formed in an environment of intracontinental stretching within a continental margin [58].

The AK metaperidotites are located southward from the high-pressure and low-pressure accretionary domains and also exhibit tectonic contact with the abovementioned units (Figure 3). Ultramafic rocks were interpreted to represent a structural extension of the Khantayshir ophiolites [59,60], but were later reported as an independent structural domain of the AK complex along with eclogites, amphibolites, and metasediments [54,61,62].

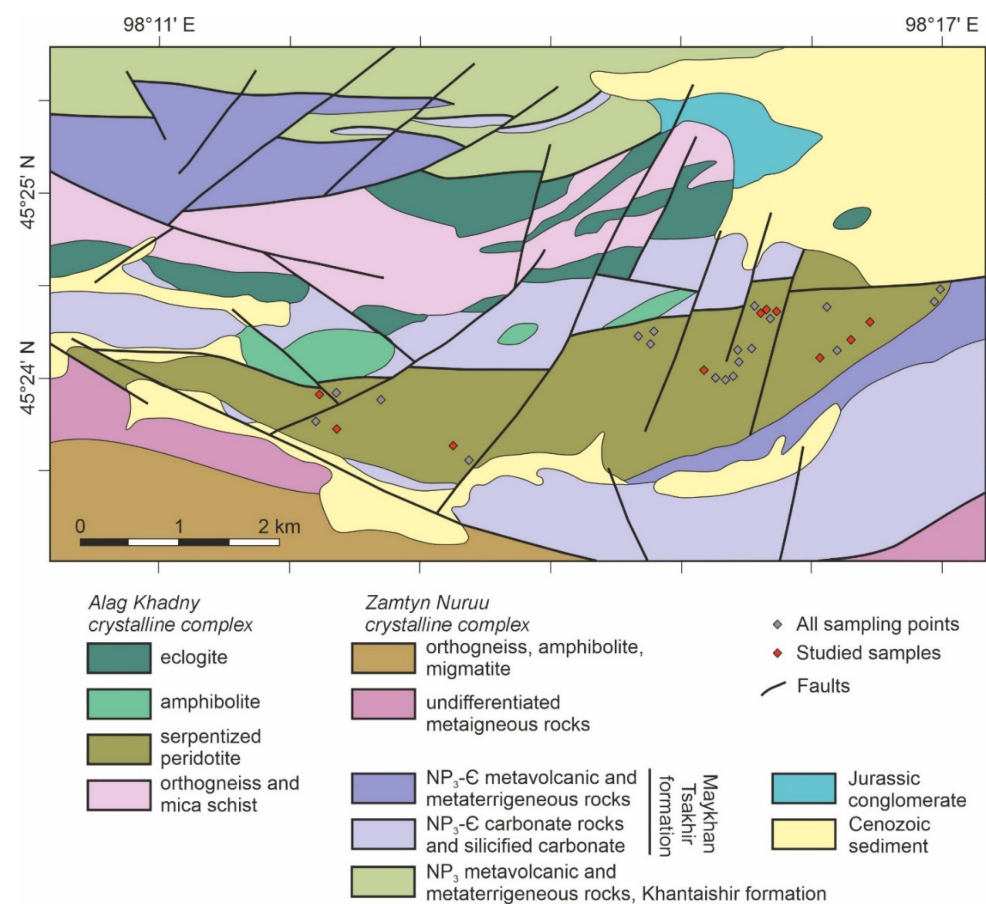


**Figure 3.** Simplified geological scheme of the Alag-Khadny accretionary complex in SW Mongolia [54,61,62] with the marked sampling locations.

Mineral assemblages and geochemical features of metaperidotites indicate the formation of source rocks in a spreading environment with later supra-subduction refertilization by melts and/or fluids and further metamorphism at P–T parameters similar to those for eclogites (640–720 °C, 1.6–2 GPa) [62]. The AK metaperidotites are represented by porphyroblastic Ol-Atg and Ol-Opx-Tr rocks with rare relics of primary silicates (Ol and Opx, and rare Cpx) (Figure 4A). Large irregularly shaped Cr-spinel grains are usually located in intergranular space (Figure 4B–D) and have metamorphic rims of variable thickness from thin ~20–100 µm (Figure 4B,C) to almost complete inward replacement of the primary Cr-spinel (Figure 4D). Smaller Cr-spinels are more rapidly replaced by Cr-magnetite rims than larger ones (Figure 4A,B). Ol is present as relics of different sizes (up to 4 mm) and

isometric to irregular in shape, with the size depending on the degree of replacement by serpentine (Atg mixed with Ctl) (Figure 4A) and by Ctl alone (Figure S1D in Supplementary File S1). Ol is often broken by serpentine aggregates into separate fragments (Figure 4A–D). Opx is present as large porphyroclasts (up to 2 mm, Figure 4F), which are almost completely replaced by pseudomorphs of metamorphic Tr, secondary Ol, and Di (Figure 4B). Atg and Ctl may also develop after these pseudomorphs (Figure S1E,F in Supplementary File S1). The Opx relics preserved in the Tr suite contain Cpx lamellae, which indicate its primary origin. Small rounded and isometric grains of metasomatic (refertilization-related) Cpx (Figure 4A) are present in almost all rocks, and their amount does not exceed the first vol.%.

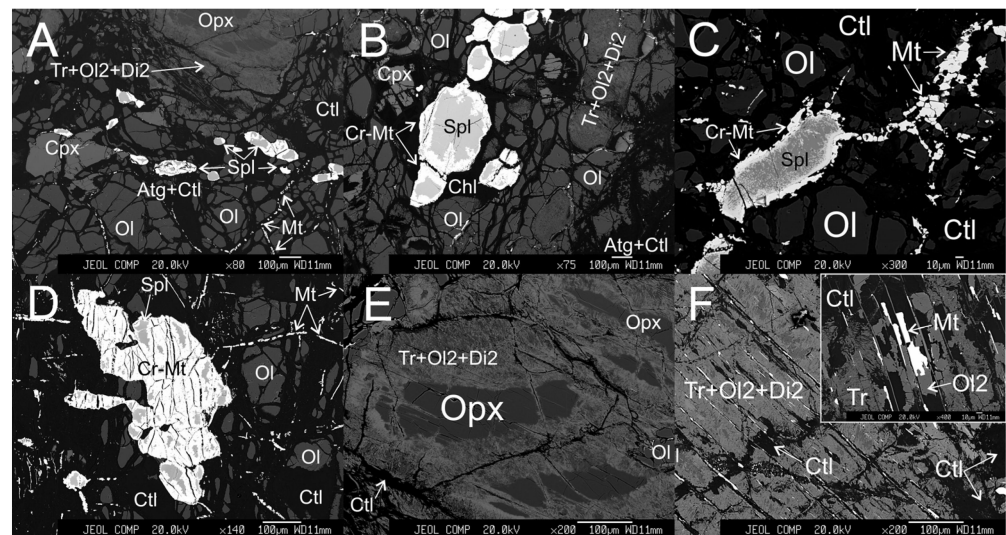


**Figure 4.** Petrographic features of metaperidotites from the Alag-Khadny accretionary complex (BSE photomicrographs). (A) An overview photo of the representative metaperidotite, M16-45, with orthopyroxene porphyroclasts completely replaced by tremolite + secondary olivine + diopside assemblage. (B) Cr-magnetite rim around a Cr-spinel grain, M16-12 metaperidotite. (C) Formation of a Cr-magnetite rim on a Cr-spinel grain, and a fine-grained aggregate of magnetite in a chrysotile matrix, M16-08 metaperidotite. (D) Replacement of primary Cr-spinel by Cr-magnetite, M16-20 metaperidotite. (E) Replacement of a large orthopyroxene porphyroclast by a tremolite + secondary olivine and diopside assemblage, with a relic of orthopyroxene in the center, M16-45 metaperidotite. (F) An enlarged fragment of the orthopyroxene replacement area, with the inset showing multiple oriented magnetite grains formed at the final stage of serpentinization, M16-29 metaperidotite.

Hydrous serpentine (including high-temperature Atg and low-temperature Ctl) and amphibole, and H<sub>2</sub>O-free secondary Ol and Di, are formed as secondary phases after primary assemblages of peridotites in both AK and KN complexes. However, the rocks exhibit distinct abundances of high- and low-temperature hydrous phases; in the KN, Atg-varieties predominate, whereas in the AK, Ctl-bearing rocks are more widespread. Atg develops along Ol margins and fractures (Figure 4E), and forms bastite after Opx; Ctl can also develop after both Ol and Opx (Figure 4A–D,F and Figure S1E,F in Supplementary File S1). Both serpentines are commonly associated with small agglomerations of magnetite. Amphibole is mainly Tr, which is closely associated with secondary Ol and secondary diopside and develops along orthopyroxene; Tr flaky aggregates are primarily oriented parallel to cleavage planes of the replaced orthopyroxene (Figure 4F). The identification of serpentine was confirmed by Raman spectroscopy (see Section 3). Serpentine from Khara-Nur and Alag-Khadny peridotites is represented by both antigorite and chrysotile (Figure S2 in Supplementary File S1).

### 3. Methods

Petrographic features and major-element composition of mineral phases in the Khara-Nur and Alag-Khadny metaperidotites were studied using a Tescan MIRA 3 LMH (Tescan,

Brno, Czech Republic) scanning electron microscope (SEM) equipped with an Oxford Instruments Ultim MAX 40 energy-dispersive (EDX) spectrometer (Oxford Instruments, Buckinghamshire, High Wycombe, UK). To reveal textural and structural features, microphotographs of polished thin sections were taken in back-scattered electron (BSE) micrographs. Mineral analyses were performed at an accelerating voltage of 20 kV, a beam current of 10 nA, and a beam diameter of  $\sim 1 \mu\text{m}$ . The time of background acquisition was 5 s at an analytical signal acquisition of 10 s. Pure Ni was used as the calibration standard. For quantitative analyses, some samples were examined by electron-probe X-ray microanalysis (EPMA) using a JEOL Superprobe JXA8200 microanalyzer (JEOL, Tokyo, Japan) at a beam size of  $2 \mu\text{m}$ , a current of 15 nA, and an accelerating voltage of 20 kV. A set of standard samples including albite for Na, pyrope garnet for Al, potassium feldspar for K, diopside for Ca, forsterite for Mg, Mn-garnet for Mn, Ti-ilmenite for Ti, and Cr-spinel for Cr were used for calibration. Sample preparation, SEM, and EPMA studies were carried out at the Center of Isotope and Geochemical Research of Vinogradov Institute of Geochemistry SB RAS [63].

The major oxide contents in the key samples were obtained using the X-ray fluorescence (XRF) method. For the analysis, rock powders ( $\sim 110 \text{ mg}$  weight) were fused with a mixture of lithium metaborate and tetraborate with the addition of LiBr solution. The determination of elemental contents was carried out using the Bruker S4 Pioneer XRF spectrometer (Bruker Corporation, Billerica, MA, USA). A detailed methodology was reported by [64]. The content of rare and trace elements was analyzed by ICP-MS on a Perkin-Elmer NexION 300D (Perkin-Elmer Corporation, Norwalk, CT, USA) quadrupole mass-spectrometer with preliminary sample preparation via acid decomposition. Powdered sample suspensions (0.05 g) were decomposed in a mixture of concentrated nitric and hydrofluoric acids (1:2) for 7 days at  $110 \text{ }^\circ\text{C}$ . A set of standard samples (SDU, BHVO-1, and JP-1) were used for controlling the accuracy and reproducibility of measurements. XRF and solution ICP-MS measurements involved equipment from the Center of Isotope and Geochemical Research IGC SB RAS as well.

The identification of serpentine varieties was performed by Raman spectroscopy using the WITec Alpha 300R confocal Raman spectrometer (Oxford Instruments, Buckinghamshire, High Wycombe, UK) equipped with a 532 nm laser and three gratings (300, 600, and 1800 grooves/mm). The laser was focused through a  $100\times$  Zeiss objective. The laser power was set to 10 mW. To estimate instrument drift, the silicon wafer was measured at least twice a day. The identification of serpentine polymorphs was performed via comparison with reference Raman spectra of serpentines from [65].

Laser-ablation-based mass-spectrometry with inductively coupled plasma (LA-ICP-MS) was applied to obtain the contents of trace elements in major silicate minerals (olivine, orthopyroxene, amphibole, and serpentine). LA-ICP-MS measurements were carried out using the Agilent 7900 (Agilent company, Santa Clara, CA, USA) quadrupole mass-spectrometer coupled to the Analyte Excite laser ablation unit (Teledyne Photon Machines, Thousand Oaks, CA, USA) with the HelEx II cell and an ArF excimer 193 nm laser. The flow values of the cooling, plasma, and Ar addition gas were 16.0, 1.0, and 1.0 L/min, respectively. Helium with a purity of 6.0 and a flow rate of 1.0 L/min was used as the carrier gas. The plasma power was 1550 W. Polished thin sections previously examined by SEM-EDX and EPMA methods were selected for analyses. All samples and standards were analyzed under the same measurement conditions, including background measurement of 20 s, sample analysis of 40 s, laser beam diameter of  $60\text{--}110 \mu\text{m}$  (as determined by the size of the analyzed phases), laser energy of  $3.51 \text{ J/cm}^2$ , and pulse frequency of 10 Hz. SRM NIST-612 silicate glass (National Institute of Standards and Technology, Gaithersburg, MD, USA) was used for the internal calibration, and BCR-2G and BHVO-2G basaltic glass standards (United States Geological Survey, Denver, CO, USA) were used for accuracy and reproducibility control of the unknowns. Elemental contents were calculated using "Iolite 4.88" software. Silicon ( $^{29}\text{Si}$ ) measured by SEM-EDX and EPMA was used as an internal standard as an element included in both the analyzed unknowns and RMs in significant amounts. In situ

trace-element measurements and Raman spectroscopic identification of serpentine-group minerals were carried out at the Center of Geodynamics and Geochronology of the Institute of the Earth's Crust SB RAS.

## 4. Results

### 4.1. The Whole-Rock Composition

Major- and trace-element compositions of metaperidotites from both KN and AK are provided in Supplementary File S2. The studied metaperidotites contain a rather large amount of volatile components, which is expressed in high LOI within 4.42–19.1 wt.% (KN) and 5.52–11.3 wt.% (AK) (Supplementary File S2). The contents of all major oxides were normalized to the anhydrous residue to avoid overlapping artifacts due to different volatile component contents. The samples of both complexes are characterized by similar ranges of  $\text{SiO}_2$  (40.2–45.8 wt.%),  $\text{FeO}$  (5.4–9.1 wt.%),  $\text{TiO}_2$  (<0.1 wt.%), and  $\text{Cr}_2\text{O}_3$  (0.24–0.84 wt.%), but distinct contents of  $\text{MgO}$  (44.5–49.2 wt.% for KN; 42.8–46.1 wt.% for AK),  $\text{Al}_2\text{O}_3$  (0.25–0.72 wt.% for KN, with one outlier of 1.7 wt.%; 0.9–1.62 wt.% for AK), and  $\text{CaO}$  (0.12–0.99 wt.% for KN; 0.18–1.86 wt.% for AK) (Supplementary File S2). In terms of  $\text{CaO-Al}_2\text{O}_3$  and  $\text{MgO/SiO}_2\text{-Al}_2\text{O}_3/\text{SiO}_2$  systematics, the composition of metaperidotites from both complexes is consistent with the same trend of progressive partial melting (Figure 5), with all samples resembling the composition of relatively depleted harzburgites (Figure 5A). Nonetheless, AK metaperidotites are characterized by higher  $\text{CaO}$  and  $\text{Al}_2\text{O}_3$  at lower  $\text{MgO}$  contents and thus are closer to the composition of the primitive mantle (PM).

A similar split is typical for rare-earth element (REE) and trace-element patterns of KN and AH metaperidotites (Figure 6). Metaperidotites from both complexes exhibit U-shaped REE patterns (Figure 6A), which are characteristic of abyssal serpentinites as, for instance, in the Mid-Atlantic Ridge East Pacific Rise at Hess Deep [66]. However, AK metaperidotites are characterized by higher chondrite-normalized REE values (0.1–2 chondrite levels) relative to KN metaperidotites (0.01–0.4 chondrite levels). According to the contents of the most conservative HREE, AK metaperidotites may represent residues from 10%–20% partial melting, whereas higher melting degrees (20%–30%) are reconstructed from KN metaperidotites. High melting degrees of peridotites from both massifs are also confirmed by comparable contents of HFSE (Ti, Zr) and Cr# Spl values [47,62].

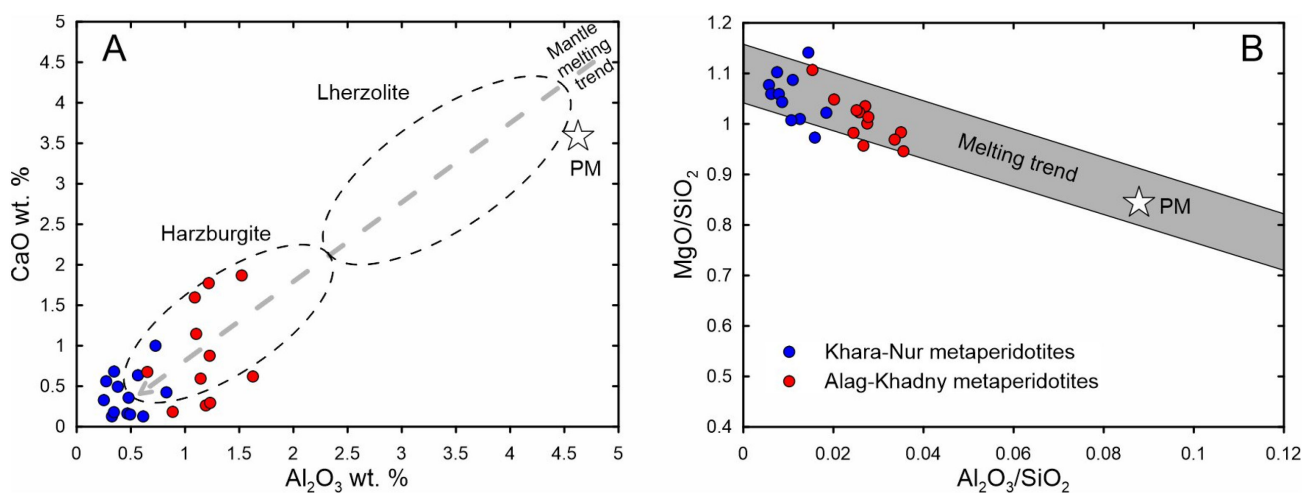


**Figure 5.** Major oxide compositions of metaperidotites from the Khara-Nur (blue circles) and Alag-Khadny (red circles) massifs, recalculated to anhydrous residues. (A)  $\text{CaO-Al}_2\text{O}_3$  systematics; (B)  $\text{MgO/SiO}_2\text{-Al}_2\text{O}_3/\text{SiO}_2$  ratios. The outlined fields mark compositions of relatively depleted harzburgites, undepleted lherzolites (both—after ([18] and refs therein)), and primitive mantle (PM) [67].

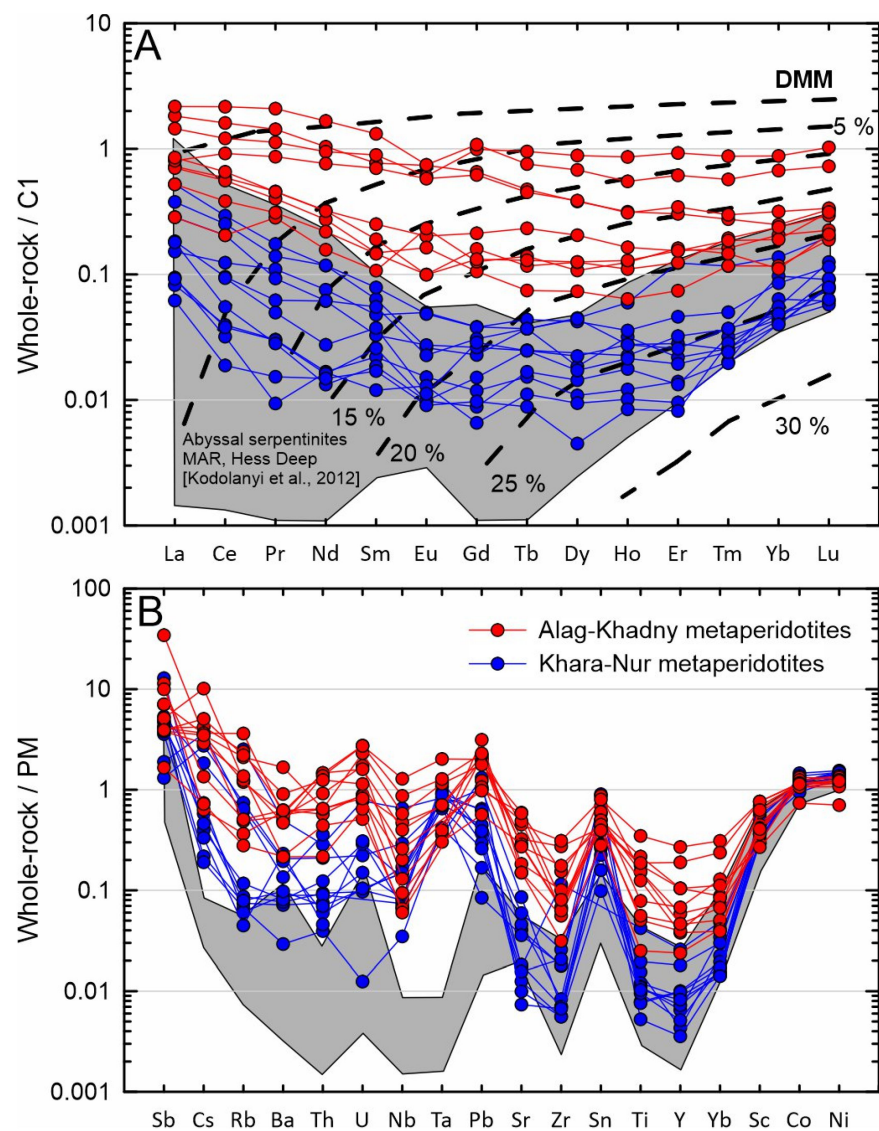


**Figure 6.** Chondrite-normalized [67] REE distribution patterns (A) and PM-normalized [67] multi-element diagrams (B) for metaperidotites of the Alag-Khadny and Khara-Nur complexes. The gray field shows the compositions of abyssal serpentinites of Hess Deep and Mid-Atlantic Ridges [68]. Dashed lines in A section mark the results of modeling of non-modal dynamic PM melting (melting equations, mineral modes, and distribution coefficients are from [69]).

The extended trace-element spectra for metaperidotites (Figure 6B) are characterized by similar shapes and differential enrichment in FMEs relative to abyssal serpentinites [68] and—in part—with respect to PM composition. The highest enrichment degrees, i.e., from 0.2–0.8 (Sr) to 1.5–30 (Sb) PM levels, are typical for the AK samples; in the KN samples, similar patterns are observed with, for instance, ~0.01–0.1 PM level contents for Sr to 1–12 PM levels for Sb. Along with that, the elemental contents and distribution patterns for slightly incompatible and relatively compatible (Yb–Ni) elements are similar in samples of both complexes and correspond to those in abyssal serpentinites (Yb–Ni) and PM (Co–Ni) (Figure 6B).

#### 4.2. In Situ Trace-Element Composition of Mineral Phases

The LA-ICP-MS in situ trace-element composition of primary Ol and Opx, serpentine-group minerals, and amphibole in the representative samples are provided in Supplementary File S2. As noted above, serpentine-group minerals (Atg and Ctl) develop after both primary

Ol and Opx, and Ctl has also been detected in large serpentine clusters as replacing Atg. To distinguish between hydrous phases, which replaced distinct primary silicates, we further label Atg and Ctl in relation to their relic phases, for example, Atg(Ol) for Atg after olivine and Ctl(Opx) for Ctl after Opx.

Trace-element patterns of Ol from AK and KN metaperidotites, as well as those from KN harzburgites and dunites, correspond to those of the New Caledonia mantle-wedge peridotites [30] and are located between Korab Kansi and Abu Dahr forearc highly depleted peridotites (25%–40% of partial melting) [70] and retrograde metaperidotites of Happon O'ne [31,71]. They are characterized by similar contents of relatively fluid-immobile HFSE and some REE (Yb, Y, Zr, and Ce) and variably mobile LILE (Sr, Pb, and Ba) elements; some Ol analyses exhibit contents below the limit of determination (LOD) (Figure 7A,B). For primary Ol from AK metaperidotites, the contents of some FMEs, such as U, W, and Sb, were determined, but for a part of the olivine analyses, most FMEs such as Cs, Rb, Ba, W, U, Pb, and Sb were still below LOD. Although KN olivines were analyzed in both metaperidotites (Ol-Opx-Tr, Ol-Tr, and Ol-Atg-Di rocks) and harzburgites and dunites, which were not affected by metamorphism, their composition is similar (Supplementary File S2).

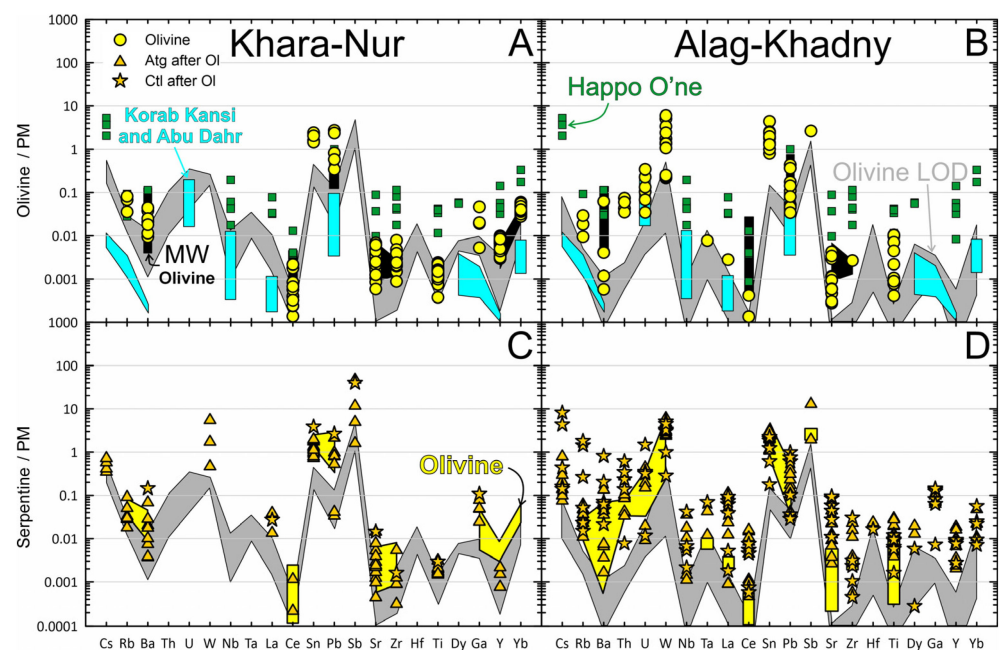


**Figure 7.** PM-normalized trace-element distribution patterns for olivine from metaperidotites (A,B) and serpentine-group minerals after Ol (C,D) [67]. MW (mantle-wedge) olivine is a field of primary olivine compositions from peridotites of the New Caledonia [29]; Happon O'ne is a field of primary olivine from Happon O'ne peridotite massif [71]; Korab Kansi and Abu Dahr—olivine compositions from of forearc highly depleted peridotite of these complexes [70]. The gray field delineates limits of determination for olivine (Olivine LOD).

The analyses of Atg(Ol) in samples from both complexes show typical inheritance from relic Ol composition in all HFSE and—in part—in FMEs, such as Rb (0.02–0.1 PM), Pb (0.01–1 PM), and Sr (0.0006–0.01 PM), but with a tendency of enrichment relative to Ol (Figure 7C,D). Atg(Ol) from KN samples shows a slight enrichment in Cs, Ba, W, and Sb (Figure 7C), while Atg(Ol) in AK samples also adds more U (Figure 7D). The only analysis of Ctl(Ol) from KN is characterized by the presence of maximum Ba (0.1 PM), Pb (3 PM), Sb (50 PM), and Sr (0.015 PM) as compared to Atg(Ol). In Ctl(Ol) from AK metaperidotites, wide compositional variations from values close to Atg(Ol) to 10 times higher Cs (10 PM), Rb (2 PM), Ba (1 PM), Sr (0.1 PM), and Ga (0.1–0.2 PM) than Ol contents are observed (Figure 7D).

Primary Opx has a trace-element composition indistinguishable from that of Ol from the New Caledonia mantle-wedge peridotites, but has lower Y (0.002–0.02 PM for KN, 0.02–0.08 PM for AK) and Yb (0.01–0.1 PM for KN, 0.04–0.1 PM for AK) contents (Figure 8A,B). Opx in both KN and AK metaperidotites have intermediate contents of the least incompatible HFSE and HREE (Zr–Yb) between Korab Kansu and Abu Dahr forearc highly depleted peridotites [70] and retrograde metaperidotites of Happon O’ne [31,71]. FMEs in Opx KN have values similar to that of Opx in the Korab Kansu and Abu Dahr metaperidotites, whereas, in AK samples, they are much higher (Figure 8A,B). Opx in AK samples is also characterized by significantly higher FME, especially that of Ba (0.6–0.9 PM), Pb (0.6–10 PM), and Sr (0.1–0.8 PM) relative to Opx of the New Caledonia peridotites (Figure 8B). Other FMEs, U and W, were also detected in Opx from AK samples but were below LOD for Opx from KN metaperidotites.

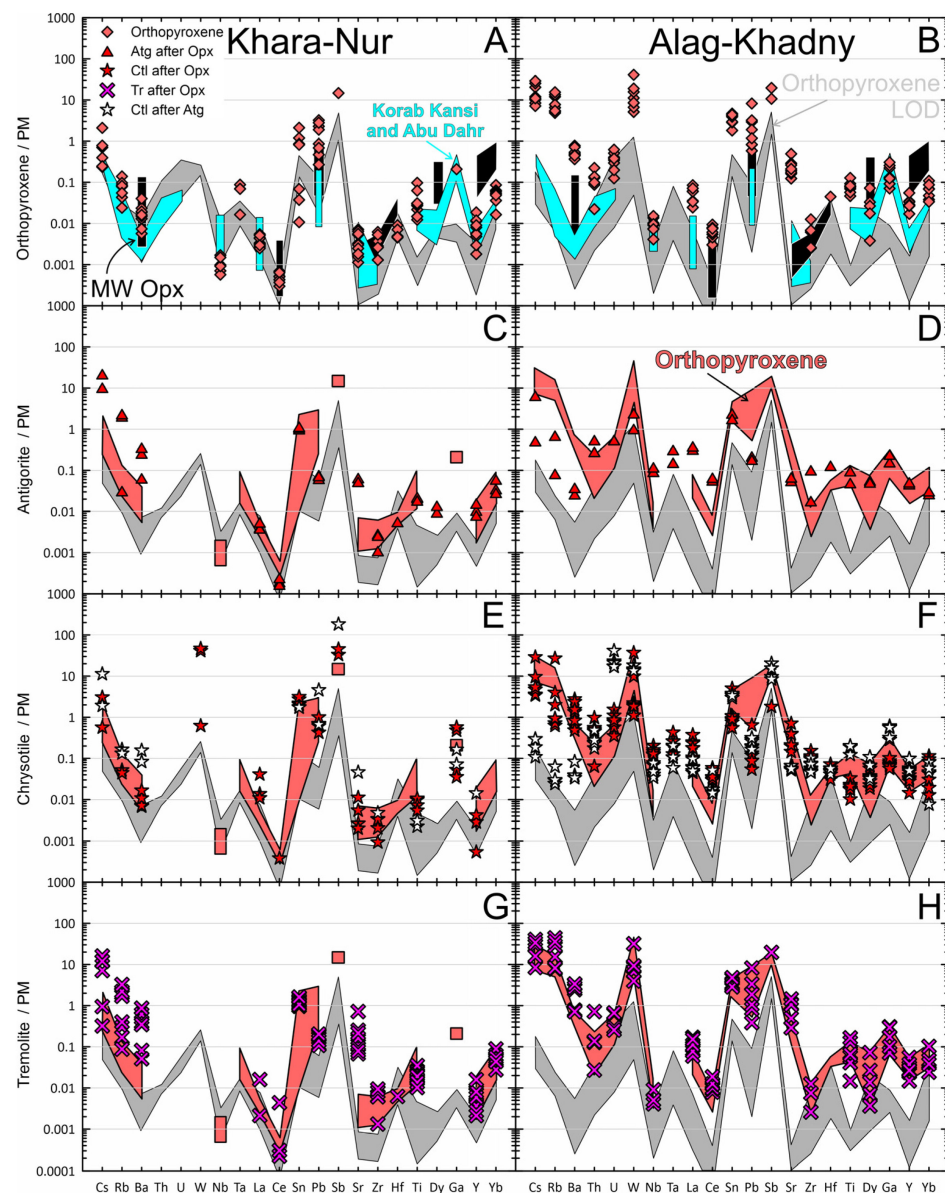


**Figure 8.** PM-normalized [67] trace-element distribution in orthopyroxene from metaperidotites (A,B), antigorite (C,D), chrysotile (E,F), and tremolite (G,H) after orthopyroxene. MW (mantle-wedge) o-pyroxene is a field of compositions of primary orthopyroxene from peridotites of the New Caledonia [29]; Korab Kansu and Abu Dahr are for orthopyroxene compositions from these highly depleted forearc peridotite massifs [70]. The gray field delineates limits of determination for orthopyroxene (Orthopyroxene LOD).

Atg(Opx) mimics the composition of primary Opx in both massifs by the distribution of moderately incompatible and HFS elements (Figure 8C,D). In KN samples, Atg(Opx) is characterized by the enrichment of FMEs (Cs, Rb, Ba, and Sr) up to 10 times and close Pb contents relative to the composition of relic Opx (Figure 8C). In contrast, Atg(Opx) has the same or lower contents of Cs, Rb, Ba, and Pb with respect to the composition of Opx (Figure 8D).

Ctl(Opx) in KN and AK rocks also inherits the composition of the relic Opx in terms of the fluid-immobile elements (Figure 8E,F), but exhibits increased contents of some FMEs (e.g., W and Sb) in KN samples, while W was not detected in Opx in KN metaperidotites. In AK metaperidotites, Ctl(Opx) demonstrates all FME contents close to that of Opx, except Pb (0.007–0.6 PM), which is lower than in Opx (Figure 8F). Trace-element patterns of Ctl(Atg) in the KN metaperidotites completely follow those of Atg but have the highest contents of Sb (>10 PM, Figure 8E). In AK samples, Ctl(Atg) also mimics the composition of Atg, except U, W, and Sb, which show the highest values (above 10 PM) (Figure 8F).

Tr in samples from both complexes replaces Opx and inherits the composition of the latter, with a tendency to increase the content of LILE (Cs, Rb, and Ba; Figure 8G,H). In KN, Tr has high Sr contents (0.08–1 PM; Figure 8G), which are ~8–10 times higher than in relic Opx and distinguish it from Tr from AK (Figure 8H).

## 5. Discussion

### 5.1. The Origin and Retrograde Hydration Conditions for AK and KN Peridotites

Residual peridotites of the Khara-Nur massif are strongly depleted (20%–30%) spinel harzburgites and dunites [47], which were interpreted to originate from the subcontinental lithospheric mantle, followed by the involvement of mantle portions into the forearc environment during initiation of the oceanic Dunzhugur paleo-arc system [72]. Within the forearc, they were subjected to metasomatism via interaction with hydrous subduction melts, which is recorded in the elevated contents of strongly incompatible elements [47]. In contrast, the AK peridotites are less depleted (10%–20%) spinel harzburgites; their formation is likely related to an extensional (mid-ocean ridge or back-arc basin) oceanic setting in the Early Neoproterozoic oceanic lithosphere. Based on trace-element modeling, AK peridotites might undergo a stage of re-melting and concurrent refertilization by percolating melts in the mantle wedge above the continental-type subduction zone [62]. In both cases, however, mantle peridotites were affected by consequent metamorphic hydration of mantle-wedge refertilization.

The primary mineral assemblage Ol-Opx-Spl is present in the metaperidotites of both massifs. In Ol-Tr ± Opx rocks, it is represented by olivine porphyroclasts (Ol1, Figure 4A), orthopyroxene relics with Cpx exsolution lamellae in large orthopyroxene pseudomorphs (Figures 2F,G and 4E), and Cr-spinel relic grain cores (Figures 2A,B and 4B–D). In Ol-Atg-Di rocks, it is represented only by Ol1 porphyroclasts and relic cores of Cr-spinels. The compositions of these minerals are the same as in suprasubduction peridotites of residual genesis (Figure 9A–D).

Metamorphic assemblages include chlorite around Sp1 (Figure 4B), metamorphic ferri-chromite either as independent grains or as rims around relic core Sp1, tremolite in association with fine metamorphic olivine (Ol2) in pseudomorphs after orthopyroxene (Figure 2G–I and Figure 4E,F), and antigorite after Ol1 and in pseudomorphs after Opx (Figure 2B,H). Ol-Atg-Di rocks of the Khara-Nur massif also contain secondary olivine (Ol2) and diopside in pseudomorphs after Opx and antigorite after Ol1 (Figure 2C). Metamorphic olivines are characterized by lower Mg# and varying NiO content (0.1–0.48 wt.%, Figure 9A) compared to primary olivine from the same samples. Metamorphic spinels have varying compositions and correspond to the compositions of ferri-chromite and magnetite of metaperidotites formed after primary Cr-spinel in the temperature range of amphibolite- to greenschist facies (Figure 9B). Notably, tremolites from the studied metaperidotites, as well as tremolites from the rehydrated Happon-O'ne rocks [31,71], have higher contents of Al<sub>2</sub>O<sub>3</sub>

(0.2–4.5 wt.%) and  $\text{Cr}_2\text{O}_3$  (0.25–1.1 wt.%), as compared to prograde tremolites (Figure 9E), which did not accumulate significant amounts of Al and Cr [28,66].

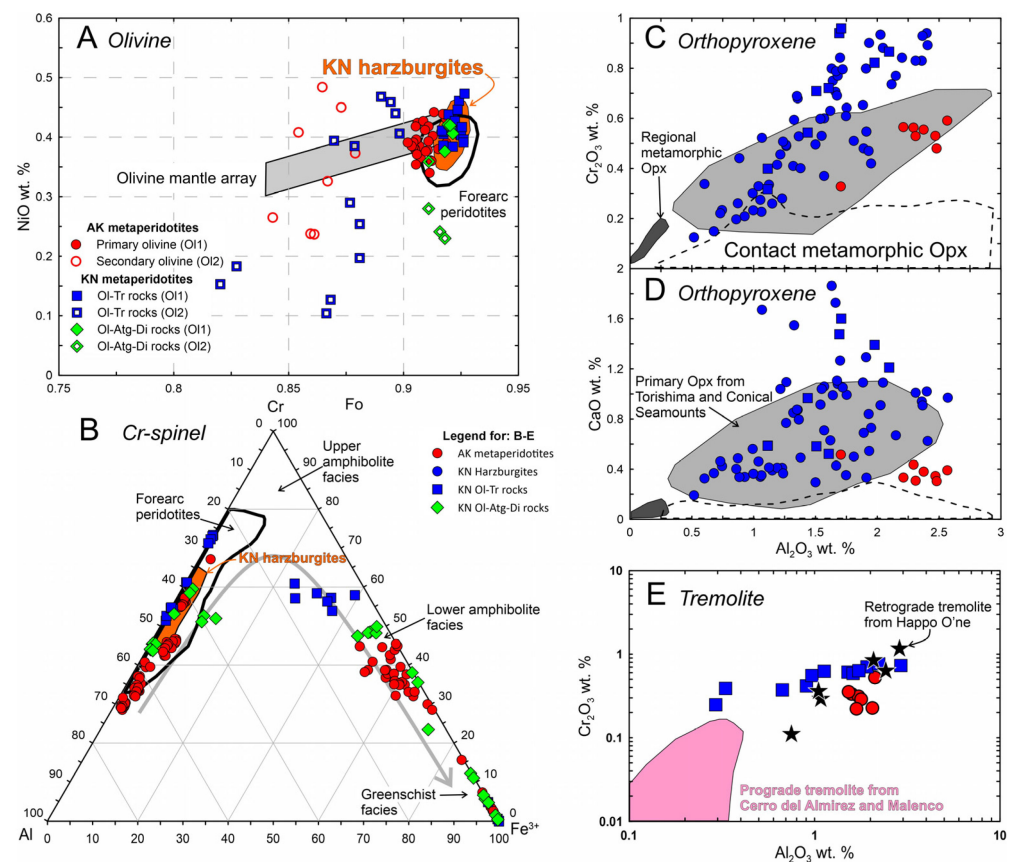
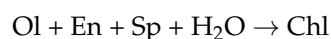


**Figure 9.** Composition of primary and secondary minerals of KN and AK metaperidotites (see also Supplementary File S2). (A) NiO content vs. Fo of olivine, O11—primary olivine, O12—secondary olivine after primary orthopyroxene. The olivine mantle array is from [73], and the field of O1 of forearc peridotites (same field as in Figure 9B) is from [74]; (B) Cr-Spinel composition in trivalent Al-Cr-Fe<sup>3+</sup> coordinates showing primary Cr-spinel and its alteration products. Thick grey line indicates a compositional trend of Cr-spinel metaperidotites during retrograde transition from upper- to lower-amphibolite and greenschist-facies conditions ([75] and references therein); (C,D) Major-element composition of orthopyroxene expressed as  $\text{Cr}_2\text{O}_3$  and CaO vs.  $\text{Al}_2\text{O}_3$  systematics. Fields of primary [74] and metamorphic Opx from regional [76,77] and contact [78] metamorphism settings are shown for comparison; (E)  $\text{Cr}_2\text{O}_3$  vs.  $\text{Al}_2\text{O}_3$  systematics of tremolite relative to compositions from the Happono O’ne retrograde tremolites [31,32] and prograde tremolite from Cerro del Almiraz and Malenco massifs [28,66].

The presence of primary mineral associations along with metamorphic minerals in the KN and AK metaperidotites indicates the retrograde nature of metamorphism during the addition of aqueous fluids to anhydrous peridotites with the formation of  $\text{Ol-Tr} \pm \text{Opx}$  and  $\text{Ol-Atg-Di}$  rocks. The composition of tremolite is consistent with this conclusion in terms of both major (Figure 9E) and trace elements (Figure 8G,H), for which direct compositional inheritance from the precursor orthopyroxene is observed. The composition of O12 formed after orthopyroxene is also consistent with the retrograde transformation model and is highlighted, for instance, by low NiO contents, as there is almost no NiO in the primary Opx (see Supplementary File S2). If O12 formed through prograde serpentine dehydration breakdown, one would expect high-Mg# compositions of the resulting olivines ( $\text{Mg}\# > 0.95$ ), as was, for example, shown for prograde O12 of the talc zone of the Happono O’ne massif [71]. Overall, the observed mineral assemblages could be formed by  $\text{H}_2\text{O}$  addition

to anhydrous harzburgites and a temperature decrease (Figure S3 in Supplementary File S1; calculated for the MgO-CaO-Al<sub>2</sub>O<sub>3</sub>-SiO<sub>2</sub>-H<sub>2</sub>O system by [79] on the basis of data [80,81]) as follows:



The assemblage of olivine + orthopyroxene + chlorite + tremolite is stable in a wide range of temperatures of 640–800 °C and pressures up to 2 GPa. The formation of talc by reaction (9) and anthophyllite by reaction (13) was not observed in the rocks of the KN and AK, but the formation of antigorite and diopside by reactions (4) and (7) was recorded (see all reactions in Figure S3 in Supplementary File S1 and in [31]). The latter is favored only in the narrow pressure range of ~1.6–2.0 GPa at ~640–720 °C. Such metamorphic conditions are commonly reproduced in mantle-wedge peridotites subjected to infiltration by hydrous fluids from the subducting plate [82]. Similar conditions (~1.6–2.0 GPa and 650–750 °C) were reported, for instance, for tremolites-bearing metaperidotites from the Happo O'ne massif [31]. For the KN metaperidotites, we identified an apparent and stepwise change in the primary mineral assemblages of the harzburgites to Ol-Tr-Opx, Ol-Tr, and Ol-Atg-Di rocks (Figure 1C), which might document a gradual approach to a former fluid-modified subduction interface. This sampled section along a ~1.5–2 km S-N traverse is located at a great distance (>2 km) from intrusive contacts (Figure 1A), which precludes thermal fluid effects from granitic or other intrusions, and thus allows us to consider the sampled metamorphic aureoles as related to different extents of subduction fluid availability.

### 5.2. Behavior of Incompatible Elements during Metamorphic Hydration

Despite numerous trace-element studies of subduction metamorphism of mantle peridotites [11–13,18,27], most research was focused on slab peridotites and subduction-channel rocks at the slab-mantle interface. Mantle peridotites in direct contact with fluid-rich crustal rocks of the slab surface are actively hydrated by subduction fluids and therefore completely serpentinized. In this case, it becomes rather difficult to estimate the effects of subduction fluids on the chemical evolution of the resulting hydrated assemblages. Upward from the plate interface, mantle-wedge peridotites experience less interaction with subduction fluids at lower fluid/rocks ratios and can preserve frozen mineral assemblages of separate hydration stages along with relics of primary silicates [32,35]. To date, there have only been a few studies that report in situ trace-element data for metamorphic minerals in mantle wedge metaperidotites, e.g., [26,30,31].

The retrograde nature of Tr, Atg, and Ctl after primary peridotitic silicates (Ol, Opx ± Cpx) [21] in both KN and AK peridotite fluid modification is favored by (1) the absence of sharp boundaries between blocks with different metamorphic assemblages and/or a consistent zonation from harzburgites to Ol-Atg-Di rocks; (2) the preservation of geochemical signatures formed by partial melting of peridotites (Figures 5 and 6); (3) the absence of textural evidence of hydrous mineral breakdown or deserpentinization (such as relics of serpentine, magnetite, and sulfides in Ol, spinifex textures, and spherulite forms) [76,78]; and (4) the presence of incomplete (“frozen”) metamorphic reactions (Figures 2 and 4) [82]. Therefore, KN and AK metaperidotites record a succession of retrograde metamorphic reactions from Opx→Tr to Ol/Opx→Atg and Ctl→Ol/Opx/Atg, with the continuous and selective inheritance of trace-element signatures from the relic phases but the gradual addition of FMEs during fluid–rock interaction. As a direct consequence of the latter, Ctl often has greater variations and higher FME contents (Figures 7 and 8) relative to the former Atg and Tr.

When comparing the composition of serpentine-group minerals in the KN and AK samples with those from metaperidotites of the Motugua and Sluna mantle wedge [30]

and the Andes [26], a few apparent similarities in FME behavior are observed (Figure 10A), including the maxima of Sb contents over adjacent Pb and Sr and an increase in normalized contents in a Ba–Rb–Cs row (Figure 10A–F). However, the absolute contents of almost all elements, including HFSE–HREE (Zr, Dy, Y, and Yb) and LILE (Cs, Rb, Ba, Pb, and Sr) (Figure 10A,B) have lower levels in Atg(Ol) and Ctl(Ol) from both complexes. Atg(Opx) from KN samples is characterized by lower HFSE contents, but comparable Cs, Rb, and Ba (Figure 10C), whereas in Atg(Opx) from AK, the whole set of elements has close values to the Motagua, Sluna, and Andean Atg, but without a maximum in Sb (Figure 10D). Ctl(Opx) and Ctl(Atg) repeat the same trends as Atg(Opx) from the corresponding massifs, but with profound Sb maxima (Figure 10E,F). Atg after Opx and Ol from progressively altered serpentinites of the Sulu terrane (subduction-channel peridotites) [11] has a similar distribution pattern of incompatible elements, but with maxima of U and Pb (Figure 10A–G), which were not observed in serpentinites of KN and AK, as well as for peridotites from the Motagua, Sluna, and Andean mantle wedges.

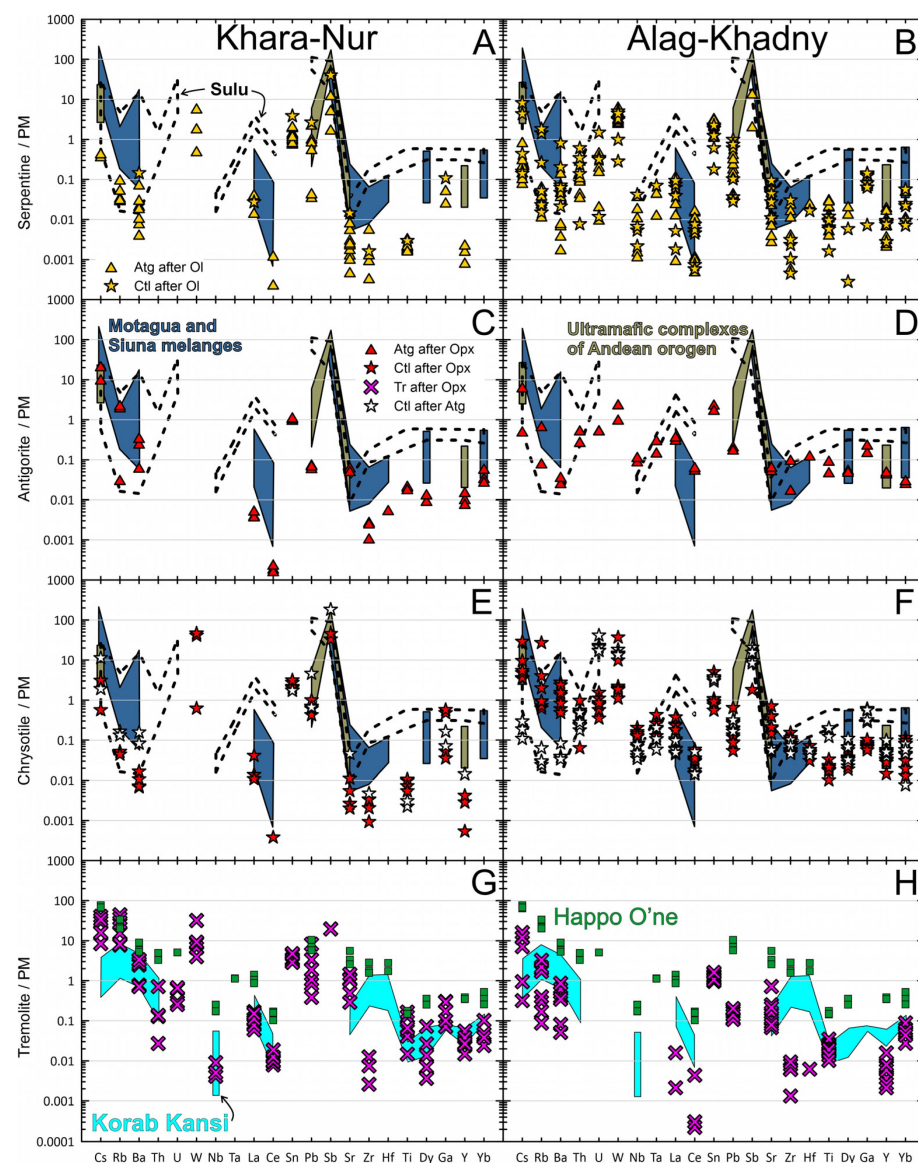


**Figure 10.** PM-normalized [67] trace-element distribution in Atg(Ol) and Ctl(Ol) (A,B), Atg(Opx) (C,D), Ctl(Opx) (E,F), and Tr (G,H) in metaperidotites from KN and AK. For comparison, the composition fields of serpentine group minerals from metaperidotites of the mantle wedge—Motagua and Sluna melanges (antigorite with small amounts of chrysotile/lizardite) [30] and ultramafic complexes of the

Andean orogen (antigorite) [34], the field of antigorite growing on olivine and orthopyroxene from the Sulu terrane (subduction channel rocks) [11] is highlighted by dots; Korab Kansi field marks compositions of secondary tremolites from forearc highly depleted serpentized harzburgites [70]; the compositions of tremolite from mantle-wedge metaperidotites of the tremolite zone of the Happon O'ne massif are shown [31,32,71].

KN and AK tremolites differ quite significantly in trace-element signatures from the Happon O'ne [31] and Korab Kansi [70] tremolites (Figure 10G,H). The tremolites of both KN and AK have lower contents of all REE and HFSE as well as Sr. The KN tremolite has comparable content of Cs, Rb, and Ba, but lower Pb (Figure 10G); in contrast, the AK tremolite has higher Cs, Rb, and Ba, and the same Pb content as the Happon O'ne tremolite (Figure 10H). A similar mechanism of metamorphic reactions was assumed for metaperidotites of the Happon O'ne massif, in which the primary mineral assemblage of peridotites was replaced by metamorphic hydration ( $\text{Tr} + \text{Di}_2 + \text{Atg} + \text{Lz}$ ) [31]. The associated changes in trace-element contents were attributed to changes in the fluid composition, and the effect of fluid addition was significant at least for LILE, REE, and—partially—some HFSE (Th, Hf).

#### 5.2.1. Fluid-Immobile HFSE

HFSE, which are slightly mobile in specific fluid environments, do not show significant variations in Atg and Ctl relative to the relic Ol and Opx, as well as to recalculated compositions of anhydrous residues (Figures 7 and 8); this is valid for both KN and AK rocks. However, the composition of primary silicates might vary before fluid impingement due to (1) different degrees of partial melting and (2) different extents of melt metasomatism and corresponding trace-element uptake (see Figures 7A,B and 6A,B). To assess the relative accumulation/loss of incompatible elements, the acquired and PM-normalized data were additionally normalized to the composition of the corresponding Ol (Figure 10) and Opx (Figure 11) relics. More specifically, uniform compositions of Ol and Opx in metaperidotites from both AK and KN allow for calculating and using their average (“within-array”) compositions. This approach makes it possible to estimate the impact of trace-element uptake from a fluid on the budget of incompatible elements in secondary minerals.

HFSE (Nb, Ta, Zr, Hf, Ti), HREE + Y (Dy, Ga, Yb), and Sn in Atg(Ol) in KN samples have lower contents relative to relic olivine or could not be quantified (Figure 11A). For Atg(Ol) in AK samples, the normalized HFSE contents are notably higher than in KN (Figure 11B), but are most likely overestimated due to the corresponding Ol values being near or below the LOD. For Ctl(Ol), the trends are similar for both complexes (Figure 11C,D). For LREE (e.g., La and Ce), the same trends as those for HFSE are preserved with no enrichment in both KN serpentine-group minerals (Figure 11A,C) and with significant enrichment in AK samples (Figure 11B,D) up to 70 times (La in Atg(Ol) and 60–70 in Ctl(Ol)). This is due to possible fractionation of LREE and HFSE in fluids, which favor the effective transport of LREE but immobile HFSE behavior [11,83]. The significant increases in La and Ce concentrations in Atg and Ctl(Ol) over those in primary Ol indicate the enrichment of subduction fluids in AK compared to KN.

In Atg(Opx) of both complexes, the trends of HFSE and LREE behavior are preserved as in the case of Atg(Ol). In KN, all values for HFSE and LREE are close to those in relic Opx (Figure 12A), except Dy, which exceeds the Opx LOD by a factor of ~10. In Opx from AK samples, almost all HFSE (except Ta) have been detected, resulting in Atg(Opx) showing no enrichment in HFSE, except for Zr (up to ~10 times) (Figure 12B). Nearly ten-fold enrichment in La and Ce for Atg(Opx) is preserved in AK samples, which confirms the above suggestion of conservative HFSE behavior in fluids in both cases and, in contrast, of differential LREE mobility in cases of continental-subduction fluids of AK.

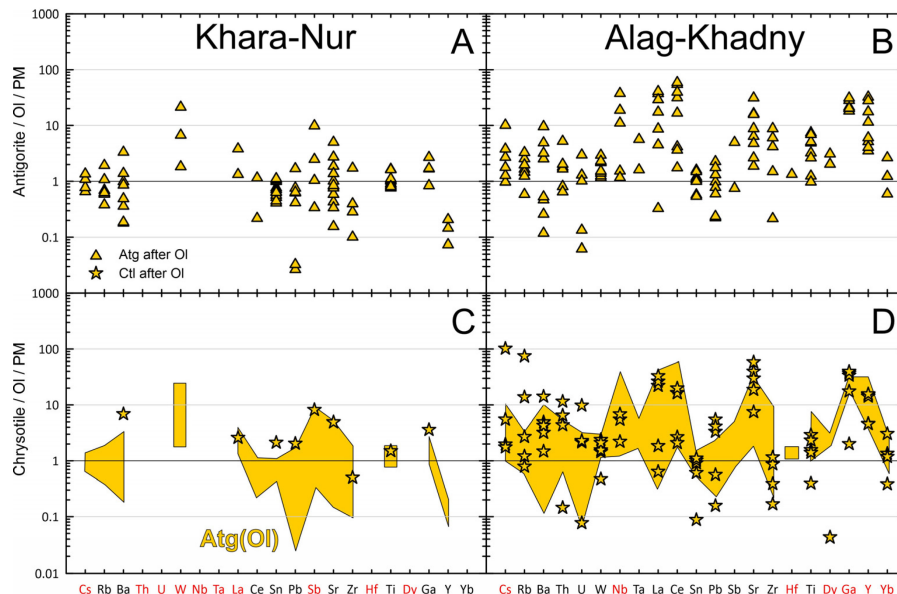


**Figure 11.** Normalized contents of trace elements in antigorite (A,B) and chrysotile (C,D) for the average composition of olivine from KN (A,C) and AK (B,D). The red color marks those elements that were not determined in the composition of Ol; in this case, the maximum LOD values calculated for Ol were used.

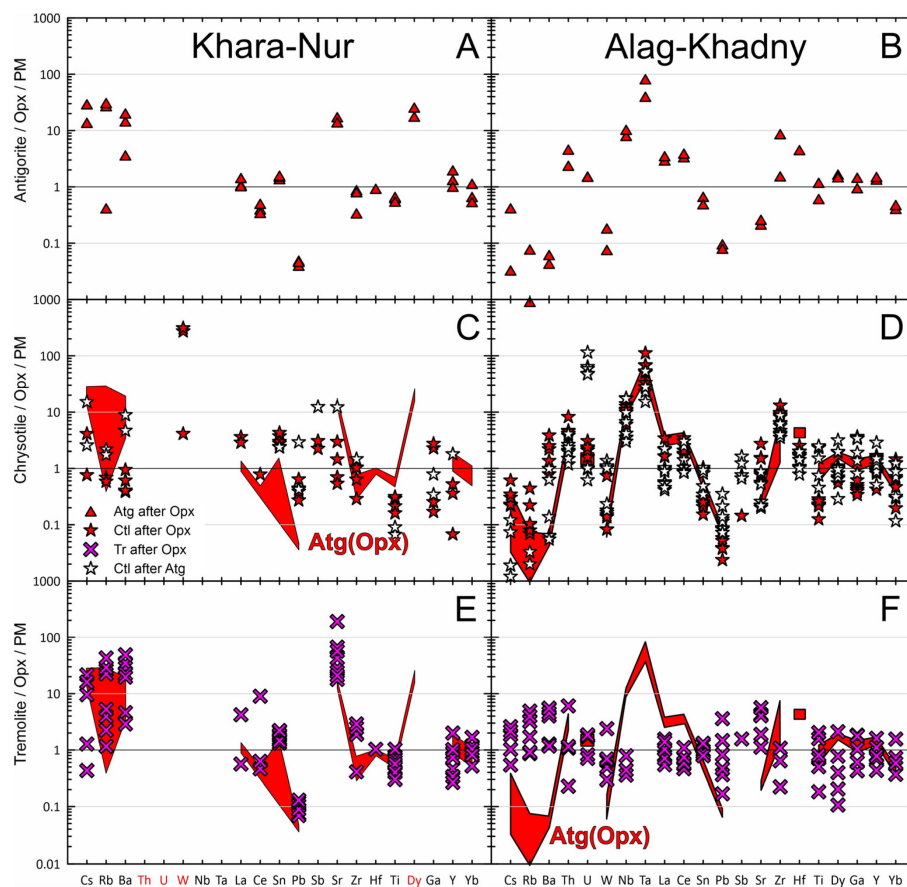


**Figure 12.** Normalized contents of trace elements in antigorite (A,B), chrysotile (C,D), and tremolite (E,F) for the average composition of orthopyroxene from KN (A,C,E) and AK (B,D,F). The red color indicates those elements that were not determined in the composition of Opx; in this case, the maximum LOD values calculated for Opx were used.

Ctl(Opx) and Ctl(Atg) follow the behavior of all HFSE for KN and AK, and, for some elements, the recalculated contents are even lower than in the precursor Atg(Opx) (Ti, Y; Figure 12C; La, Ce, Hf; Figure 12D). In AK samples, only Zr exhibits the maximum (up to ~20 times relative to Opx; Figure 12D) and corresponds to such contents in Atg(Opx). According to recent experimental studies, the HFSE group (Zr, Nb, Ta, and Hf) can be partially remobilized in supercritical fluids [84], which should not be the case for relatively low-temperature (~600–720 °C) high-pressure AK rocks. Although Zr was reported to have the highest fluid mobility because of its highest fluid/melt partitioning coefficient among HFSE ( $0.3 \pm 0.1$ ) [85], the fact and reasons behind Zr enrichment should be investigated further and in more detail.

The tremolite after Opx in KN and AK rocks does not show significant variations of HFSE contents relative to the relic Opx; the only observation of the increase in La and Ce is observed in KN (Figure 12E,F). Overall, Tr HSE patterns almost completely follow the composition of the precursor Opx.

### 5.2.2. Fluid-Mobile Elements in Retrograde Hydration Processes

FME (Cs, Rb, Ba, U, W, Pb, Sb, Sr  $\pm$  La, and Ce) enrichment/depletion in metaperidotites may be governed by both pre-metamorphic processes, such as partial melting (and accompanying FME loss) and melt-peridotite interactions and the extent of FME uptake from the available metamorphic fluids. However, both high degrees (>10%) (Figure 6) of partial melting and low residual FME contents of primary silicates do not favor the inheritance of FME signatures from Ol and Opx. Thus, the FME budget in the AK and KN metaperidotites will be mainly controlled by metamorphic fluid addition and its chemistry.

Atg(Ol) is characterized by different levels of FME abundance relative to relic olivine (Figure 11A,B). In KN samples, W shows the highest levels of accumulation (up to ~20 times relative to LOD in Ol), whereas Sr shows high variability (0.1–10 times), and the remaining FMEs exhibit limited mobility (Figure 11A). In contrast, almost all FMEs in AK samples have higher contents relative to relic Ol, but Cs–Ba (up to a 10 times), LREE (up to 80 times), and Sr (up to 40 times) show the highest enrichment (Figure 11B). One analysis of Ctl(Ol) in KN rocks shows only an increase in Ba (up to ~8 times) relative to the relic Opx and Atg(Ol) compositions, while the rest of the FMEs are within the Atg(Ol) field (Figure 11C). In AK metaperidotites, Ctl(Ol) has either similar or slightly higher FME (Cs, Rb, Ba, U, Pb, and Sr) contents relative to Atg(Ol) (Figure 11D).

Atg(Opx) in KN metaperidotites is enriched in Cs, Rb, Ba, and Sr by 10–30 times and depleted in Pb (by 30–40 times) relative to Opx (Figure 12A). In contrast, Atg(Opx) in AK shows Cs, Rb, Ba, and Sr depletion (5–50 times, and up to 1000 times for Rb; Figure 12B). Ctl(Opx) and Ctl(Atg) in both KN and AK basically reproduce the same FME variations as the corresponding Atg(Opx) does, with differences only in elevated contents of W (up to ~200 times the LOD in Opx from KN samples; Figure 12C) and U (up to ~150 times the LOD in Opx from AK samples; Figure 12D). Tr in KN is strongly enriched in Cs, Rb, Ba, and Sr (10 to 200 times relative to the composition of relic Opx, Figure 12E) and, in general, has similar distribution patterns of incompatible elements to that of Atg(Opx). Tr in AK rocks does not show large variations in FME contents relative to Opx, as they vary upward and downward by a factor of no more than 8 (Figure 12F).

An obvious inconsistency in the distribution patterns of all incompatible elements and, to a greater extent, FMEs between metamorphic phases is the evidence of higher relative contents in phases formed through Ol  $\rightarrow$  Atg/Ctl in AK metaperidotites (Figure 11B,D) than those in Opx replacement reactions (Figure 12B,D,F). Importantly, KN metaperidotites exhibit the opposite pattern (Figure 12A,C,E), where relative FME contents are higher in secondary hydrous phases formed through Opx breakdown (Figure 11A,C). According to experimental data on the serpentinization of peridotitic minerals, e.g., [86], the intensity of fluid-induced replacement reversely correlates with the amount of Al. At low Al contents, the process of Opx replacement is enhanced several times, while the opposite trend is typical of Ol. As KN metaperidotites bear relatively Al-poor Opx (0.2–2.5 wt.% in KN

vs. 2–3 wt.% in AK [47,62], the enhanced Opx replacement by hydrous minerals could be several times higher in KN rocks than in AK and might account for increased contents of some FMEs in Atg(Opx) of KN.

During subduction, mantle-wedge peridotites undergo hydration by slab-derived fluids from the subducted oceanic or continental lithosphere. From natural observations, at relatively high pressures and depths (60–90 km, 1.5–3.0 GPa), subducted crustal rocks release large amounts of FMEs (Cs, Rb, Ba, U, Pb, Sr, and LREE) into hydrous fluids [6,87]. Correspondingly, on the course of fluid migration en route upwards, this FME cargo may be variably incorporated by high-temperature Tr + Atg assemblages. This is consistent with observations in this study (see Figures 7 and 8), with the important evidence of (1) more prominent FME enrichment in AK metaperidotites and (2) preferential enrichment by some apparent markers (e.g., Th and U) of continental-crust dehydration recorded by Tr and Atg from AK rocks (Figures 7D and 8D,F,H). At lower pressures and depths, the solubility of Sb increases [11,88], causing its more active incorporation into Ctl with respect to Atg/Tr (Figures 11 and 12). Although the mobility of different FMEs may depend on particular P–T conditions of slab dehydration, the resulting enrichment of subduction fluids and hydrous minerals produced depend more on their source lithologies. As it was shown, for instance, for serpentinites from Northern Tibet [88], the introduction of continental lithosphere into a subduction zone leads to higher FME extraction to associated fluids and the relative FME (e.g., Rb, Ba, Sr) enrichment of hydrous assemblages with respect to oceanic subduction settings [11,19,88]. Thus, the obtained data from the Khara-Nur and Alag-Khadny metaperidotites clearly demonstrate that the patterns of FME enrichment, including the mobility of relatively fluid-immobile elements (e.g., Th and LREE), in suprasubduction metaperidotites may be governed by the composition of subducted and dehydrated lithologies (either oceanic or continental).

## 6. Conclusions

We have carried out a comparative analysis of the in situ trace-element composition of silicate minerals in primary dry assemblages (olivine and orthopyroxene) and metamorphic hydrous phases (tremolite, antigorite, and chrysotile) in mantle-wedge metaperidotites, which were formed in subduction regimes—oceanic for metaperidotites of Khara-Nur (Eastern Sayan) and continental for Alag Khadny (southwestern Mongolia). Hydrous metamorphic minerals were considered to have formed through replacement reactions after olivine (Atg(Ol) and Ctl(Ol)) and orthopyroxene (Tr, Atg(Opx), Ctl(Opx)).

During metamorphic hydration in similar P–T conditions, the behavior of conservative HFSE and—in part—HREE (Zr, Nb, Ta, Ti, Y, and Yb) does not distinguish between the two types of subduction environments. Primary serpentinization of mantle peridotites leads to orthopyroxene replacement with the formation of tremolite, followed by olivine replacement and the formation of antigorite (250–600 °C). Further chrysotile formation (<250 °C) can occur both due to serpentinization of the remaining pyroxenes [89] and due to partial phase transformation of antigorite into chrysotile [31]. Selective enrichment of some fluid-immobile elements (e.g., Zr) may occur in response to the latter, but should be further investigated in more detail.

Distinct patterns of FME enrichment in tremolite and antigorite from Khara-Nur and Alag Khadny relative to their primary minerals indicate different sequences of fluid-induced replacement, which started from olivine breakdown in the Alag Khadny metaperidotites and from Opx replacement in Khara-Nur, being controlled by Opx composition.

Different patterns and degrees of FME enrichment in metaperidotites reflect variations in metamorphic fluid composition in the two complexes, which was primarily governed by the contrasting nature of subducted lithologies. The affinity of Alag-Khadny to subduction of a continental margin is recorded by generally increased FME contents and selective enrichment by some moderately mobile elements, such as U, Th, and LREE, with respect to the oceanic-type subduction environment of Khara-Nur. The evaluation of the initial composition of the protolith and precursor minerals affected by multi-stage melting and

melt metasomatism may be critical and should be considered in the estimates of the differential fluid overprint and associated elemental uptake from subduction fluids.

**Supplementary Materials:** The following supporting information can be downloaded at: <https://www.mdpi.com/article/10.3390/min14050457/s1>, File S1: Figure S1: Transmitted and reflected light images of polished slices of metaperidotite KN (A–C) and AK (D–F); Figure S2: Representative Raman spectra of serpentines; Figure S3: P–T conditions of metamorphism of the Khara-Nur and Alag Khadny peridotites. File S2: Whole-rock analysis and in situ major and trace elements analysis of minerals.

**Author Contributions:** Conceptualization, A.A.K. and M.A.G.; Methodology, A.A.K., V.A.B. and S.Y.S.; Investigation, A.A.K., M.A.G. and V.A.B.; Formal Analysis, V.A.B. and N.V.B.; Writing—Original Draft Preparation, A.A.K., M.A.G. and V.A.B.; Writing—Review and Editing, M.A.G., S.Y.S. and A.Y.M.; Project Administration and Funding Acquisition, S.Y.S. All authors have read and agreed to the published version of the manuscript.

**Funding:** This study was supported by the Russian Science Foundation (Grant 21-77-10038 to SS, <https://rscf.ru/project/21-77-10038/>, accessed on 28 March 2024).

**Data Availability Statement:** Data are contained within the article and Supplementary Materials.

**Acknowledgments:** The authors thank to two anonymous reviewers helped to improve the article considerably.

**Conflicts of Interest:** The authors declare no conflict of interest.

## References

1. Zindler, A.; Hart, S. Chemical Geodynamics. *Annu. Rev. Earth Planet. Sci.* **1986**, *14*, 493–571. [[CrossRef](#)]
2. Stracke, A. Earth's Heterogeneous Mantle: A Product of Convection-Driven Interaction between Crust and Mantle. *Chem. Geol.* **2012**, *330–331*, 274–299. [[CrossRef](#)]
3. Stracke, A. A Process-Oriented Approach to Mantle Geochemistry. *Chem. Geol.* **2021**, *579*, 120350. [[CrossRef](#)]
4. Zheng, J.; Xiong, Q.; Zhao, Y.; Li, W. Subduction-Zone Peridotites and Their Records of Crust-Mantle Interaction. *Sci. China Earth Sci.* **2019**, *62*, 1033–1052. [[CrossRef](#)]
5. Zheng, Y.-F. Subduction Zone Geochemistry. *Geosci. Front.* **2019**, *10*, 1223–1254. [[CrossRef](#)]
6. Bebout, G.E. Metamorphic Chemical Geodynamics of Subduction Zones. *Earth Planet. Sci. Lett.* **2007**, *260*, 373–393. [[CrossRef](#)]
7. Yin, Z.-Z.; Chen, R.-X.; Zheng, Y.-F.; Gong, B.; Zha, X.-P.; Xia, X. Serpentinization and Deserpentinization of the Mantle Wedge at a Convergent Plate Margin: Evidence of Orogenic Peridotites from a Composite Oceanic–Continental Subduction Zone. *J. Petrol.* **2023**, *64*, egad015. [[CrossRef](#)]
8. Deschamps, F.; Godard, M.; Guillot, S.; Chauvel, C.; Andreani, M.; Hattori, K.; Wunder, B.; France, L. Behavior of Fluid-Mobile Elements in Serpentines from Abyssal to Subduction Environments: Examples from Cuba and Dominican Republic. *Chem. Geol.* **2012**, *312–313*, 93–117. [[CrossRef](#)]
9. Deschamps, F.; Godard, M.; Guillot, S.; Hattori, K. Geochemistry of Subduction Zone Serpentinites: A Review. *Lithos* **2013**, *178*, 96–127. [[CrossRef](#)]
10. Evans, B.W.; Hattori, K.; Baronnet, A. Serpentinite: What, Why, Where? *Elements* **2013**, *9*, 99–106. [[CrossRef](#)]
11. Xie, Z.; Hattori, K.; Dong, Y.; Wang, J. In Situ Characterization of Forearc Serpentinized Peridotite from the Sulu Ultrahigh-Pressure Terrane: Behavior of Fluid-Mobile Elements in Continental Subduction Zone. *Geosci. Front.* **2021**, *12*, 101139. [[CrossRef](#)]
12. Hirauchi, K.; Segawa, I.; Kouketsu, Y.; Harigane, Y.; Ohara, Y.; Snow, J.; Sen, A.; Fujii, M.; Okino, K. Alteration Processes Recorded by Back-arc Mantle Peridotites from Oceanic Core Complexes, Shikoku Basin, Philippine Sea. *Isl. Arc* **2021**, *30*, e12419. [[CrossRef](#)]
13. Tichadou, C.; Godard, M.; Muñoz, M.; Labaume, P.; Vauchez, A.; Gaucher, E.C.; Calassou, S. Mineralogical and Geochemical Study of Serpentinized Peridotites from the North-Western Pyrenees: New Insights on Serpentinization along Magma-Poor Continental Passive Margins. *Lithos* **2021**, *406–407*, 106521. [[CrossRef](#)]
14. Scambelluri, M.; Pettko, T.; Cannà, E. Fluid-Related Inclusions in Alpine High-Pressure Peridotite Reveal Trace Element Recycling during Subduction-Zone Dehydration of Serpentinized Mantle (Cima Di Gagnone, Swiss Alps). *Earth Planet. Sci. Lett.* **2015**, *429*, 45–59. [[CrossRef](#)]
15. Scambelluri, M.; Cannà, E.; Gilio, M. The Water and Fluid-Mobile Element Cycles during Serpentinite Subduction. A Review. *Eur. J. Mineral.* **2019**, *31*, 405–428. [[CrossRef](#)]
16. Cannà, E. Boron Isotope Fractionation in Subducted Serpentinites: A Modelling Attempt. *Lithos* **2020**, *376–377*, 105768. [[CrossRef](#)]
17. Deschamps, F.; Guillot, S.; Godard, M.; Chauvel, C.; Andreani, M.; Hattori, K. In Situ Characterization of Serpentinites from Forearc Mantle Wedges: Timing of Serpentinization and Behavior of Fluid-Mobile Elements in Subduction Zones. *Chem. Geol.* **2010**, *269*, 262–277. [[CrossRef](#)]

18. Lafay, R.; Baumgartner, L.P.; Delacour, A. Preservation of mantle heterogeneities and serpentinization signature during antigorite dehydration: The example of the Bergell contact aureole. *Journ. Of Metamorph. Geol.* **2023**, *41*, 377–399. [[CrossRef](#)]
19. Hattori, K.H.; Guillot, S. Geochemical Character of Serpentinites Associated with High- to Ultrahigh-Pressure Metamorphic Rocks in the Alps, Cuba, and the Himalayas: Recycling of Elements in Subduction Zones. *Geochem. Geophys. Geosyst.* **2007**, *8*, 1–27. [[CrossRef](#)]
20. Ulmer, P.; Trommsdorff, V. Serpentine Stability to Mantle Depths and Subduction-Related Magmatism. *Science* **1995**, *268*, 858–861. [[CrossRef](#)] [[PubMed](#)]
21. Bucher, K.; Grapes, R.H.; Winkler, H.G.F. *Petrogenesis of Metamorphic Rocks*, 8th ed.; Springer: Berlin/Heidelberg, Germany; New York, NY, USA, 2011; ISBN 978-3-540-74168-8.
22. Schwartz, S.; Guillot, S.; Reynard, B.; Lafay, R.; Debret, B.; Nicollet, C.; Lanari, P.; Auzende, A.L. Pressure–Temperature Estimates of the Lizardite/Antigorite Transition in High Pressure Serpentinites. *Lithos* **2013**, *178*, 197–210. [[CrossRef](#)]
23. Nozaka, T. Metamorphic History of Serpentine Mylonites from the Happo Ultramafic Complex, Central Japan. *J. Metamorph. Geol.* **2005**, *23*, 711–723. [[CrossRef](#)]
24. Sills, J.D. The Retrogression of Ultramafic Granulites from the Scourian of NW Scotland. *Mineral. Mag.* **1982**, *46*, 55–61. [[CrossRef](#)]
25. Mével, C. Serpentinization of Abyssal Peridotites at Mid-Ocean Ridges. *Comptes Rendus Geosci.* **2003**, *335*, 825–852. [[CrossRef](#)]
26. Silantyev, S.A.; Krasnova, E.A.; Badyukov, D.D.; Zhilkina, A.V.; Kuzmina, T.G.; Gryaznova, A.S.; Shcherbakov, V.D. Carbonation of Serpentinites of the Mid-Atlantic Ridge: 1. Geochemical Trends and Mineral Assemblages. *Petrology* **2022**, *30*, S25–S52. [[CrossRef](#)]
27. Marchesi, C.; Garrido, C.J.; Bosch, D.; Bodinier, J.-L.; Gervilla, F.; Hidas, K. Mantle Refertilization by Melts of Crustal-Derived Garnet Pyroxenite: Evidence from the Ronda Peridotite Massif, Southern Spain. *Earth Planet. Sci. Lett.* **2013**, *362*, 66–75. [[CrossRef](#)]
28. Pettke, T.; Bretscher, A. Fluid-Mediated Element Cycling in Subducted Oceanic Lithosphere: The Orogenic Serpentine Perspective. *Earth-Sci. Rev.* **2022**, *225*, 103896. [[CrossRef](#)]
29. Ulrich, M.; Muñoz, M.; Boulvais, P.; Cathelineau, M.; Cluzel, D.; Guillot, S.; Picard, C. Serpentinization of New Caledonia Peridotites: From Depth to (Sub-)Surface. *Contrib. Miner. Pet.* **2020**, *175*, 91. [[CrossRef](#)]
30. Martin, C.; Flores, K.E.; Vitale-Brovarone, A.; Angiboust, S.; Harlow, G.E. Deep Mantle Serpentinization in Subduction Zones: Insight from in Situ B Isotopes in Slab and Mantle Wedge Serpentinites. *Chem. Geol.* **2020**, *545*, 119637. [[CrossRef](#)]
31. Khedr, M.Z.; Arai, S. Hydrous Peridotites with Ti-Rich Chromian Spinel as a Low-Temperature Forearc Mantle Facies: Evidence from the Happo-One Metaperidotites (Japan). *Contrib. Miner. Pet.* **2010**, *159*, 137–157. [[CrossRef](#)]
32. Khedr, M.Z.; Arai, S.; Tamura, A.; Morishita, T. Clinopyroxenes in High-P Metaperidotites from Happo-O’ne, Central Japan: Implications for Wedge-Transversal Chemical Change of Slab-Derived Fluids. *Lithos* **2010**, *119*, 439–456. [[CrossRef](#)]
33. Savelieva, G.N.; Raznitsin, Y.N.; Merkulova, M.V. Metamorphism of Peridotites in the Mantle Wedge above the Subduction Zone: Hydration of the Lithospheric Mantle. *Dokl. Earth Sci.* **2016**, *468*, 438–440. [[CrossRef](#)]
34. Donoso-Tapia, D.; Flores, K.E.; Martin, C.; Gazel, E.; Marsh, J. Exhumed Serpentinites and Their Tectonic Significance in Non-Collisional Orogens. *Geochem. Geophys. Geosyst.* **2024**, *25*, e2023GC011072. [[CrossRef](#)]
35. Savov, I.P.; Ryan, J.G.; D’Antonio, M.; Kelley, K.; Mattie, P. Geochemistry of Serpentinized Peridotites from the Mariana Forearc Conical Seamount, ODP Leg 125: Implications for the Elemental Recycling at Subduction Zones: Serpentinized Peridotites. *Geochem. Geophys. Geosyst.* **2005**, *6*, 1–24. [[CrossRef](#)]
36. Dobretsov, N.L.; Buslov, M.M.; Vernikovskiy, V.A. Neoproterozoic to Early Ordovician Evolution of the Paleo-Asian Ocean: Implications to the Break-up of Rodinia. *Gondwana Res.* **2003**, *6*, 143–159. [[CrossRef](#)]
37. Furnes, H.; Safonova, I. Ophiolites of the Central Asian Orogenic Belt: Geochemical and Petrological Characterization and Tectonic Settings. *Geosci. Front.* **2019**, *10*, 1255–1284. [[CrossRef](#)]
38. Kuzmichev, A.B. *Tectonic History of the Tuva-Mongolian Massif: Easrly Baikalian, Late Baikalian and Early Caledonian Stages*; PROBEL: Moscow, Russia, 2004.
39. Štípská, P.; Schulmann, K.; Lehmann, J.; Corsini, M.; Lexa, O.; Tomurhuu, D. Early Cambrian Eclogites in SW Mongolia: Evidence That the Palaeo-Asian Ocean Suture Extends Further East than Expected: Cambrian Eclogites in SW Mongolia. *J. Metamorph. Geol.* **2010**, *28*, 915–933. [[CrossRef](#)]
40. Skuzovatov, S.Y.; Shatsky, V.S.; Dril, S.I.; Perepelov, A.B. Elemental and Isotopic (Nd-Sr-O) Geochemistry of Eclogites from the Zamtyn-Nuruu Area (SW Mongolia): Crustal Contribution and Relation to Neoproterozoic Subduction-Accretion Events. *J. Asian Earth Sci.* **2018**, *167*, 33–51. [[CrossRef](#)]
41. Donskaya, T.V.; Gladkochub, D.P.; Mazukabzov, A.M.; Ivanov, A.V. Late Paleozoic—Mesozoic Subduction-Related Magmatism at the Southern Margin of the Siberian Continent and the 150 Million-Year History of the Mongol-Okhotsk Ocean. *J. Asian Earth Sci.* **2013**, *62*, 79–97. [[CrossRef](#)]
42. Dobretsov, N.L.; Konnikov, E.G.; Medvedev, V.N.; Sklyarov, E.V. Ophiolites and olistostromes of Eastern Sayan. In *Riphean—Early Paleozoic Ophiolites of Northern Eurasia*; Nauka: Novosibirsk, Russia, 1985; pp. 34–58.
43. Sklyarov, E.V.; Kovach, V.P.; Kotov, A.B.; Kuzmichev, A.B.; Lavrenchuk, A.V.; Perelyaev, V.I.; Shchipansky, A.A. Boninites and Ophiolites: Problems of Their Relations and Petrogenesis of Boninites. *Russ. Geol. Geophys.* **2016**, *57*, 127–140. [[CrossRef](#)]
44. Dilek, Y.; Furnes, H. Ophiolite Genesis and Global Tectonics: Geochemical and Tectonic Fingerprinting of Ancient Oceanic Lithosphere. *Geol. Soc. Am. Bull.* **2011**, *123*, 387–411. [[CrossRef](#)]

45. Furnes, H.; Dilek, Y. Geochemical Characterization and Petrogenesis of Intermediate to Silicic Rocks in Ophiolites: A Global Synthesis. *Earth-Sci. Rev.* **2017**, *166*, 1–37. [[CrossRef](#)]
46. Belyaev, V.A.; Wang, K.-L.; Gornova, M.A.; Dril', S.I.; Karimov, A.A.; Medvedev, A.Y.; Noskova, Y.V. Geochemistry and Origin of the Eastern Sayan Ophiolites, Tuva-Mongolian Microcontinent (Southern Siberia). *Geodyn. Tektonophys.* **2017**, *8*, 411–415. [[CrossRef](#)]
47. Gornova, M.A.; Belyaev, V.A.; Karimov, A.A.; Skuzovatov, S.Y.; Karmanov, N.S.; Medvedev, A.Y.; Bryanskiy, N.V. Supra-Subduction Melt Modification of the Fossil Subcontinental Lithospheric Mantle: Insights from Ultra-Depleted Khara-Nur Ophiolitic Peridotites (Eastern Sayan, Central Asian Orogenic Belt). *Front. Earth Sci.* **2023**, *11*, 1270053. [[CrossRef](#)]
48. Suturin, A.N. *Geochemistry of Ultramafic Rocks of Eastern Sayan*; Nauka: Novosibirsk, Russia, 1978.
49. Kuzmichev, A.B. Neoproterozoic Accretion of the Tuva-Mongolian Massif, One of the Precambrian Terranes in the Central Asian Orogenic Belt. In *Composition and Evolution of Central Asian Orogenic Belt: Geology, Evolution, Tectonics, and Models*; Borntraeger Science Publishers: Stuttgart, Germany, 2015; pp. 66–92.
50. Kröner, A.; Kovach, V.; Alexeiev, D.; Wang, K.-L.; Wong, J.; Degtyarev, K.; Kozakov, I. No Excessive Crustal Growth in the Central Asian Orogenic Belt: Further Evidence from Field Relationships and Isotopic Data. *Gondwana Res.* **2017**, *50*, 135–166. [[CrossRef](#)]
51. Skopintsev, V.G.; Skopintseva, E.V.; Ivlev, A.S.; Kapitalinina, L.L.; Katyukha, Y.P.; Bednenko, N.Y. *State Geological Map of Russian Federation, Scale 1:200,000, Sheet N-47-XXXV. Explanatory Note*; Moscow Branch of VSEGEI: Moscow, Russia, 2021; ISBN 978-5-00193-084-6.
52. Kozakov, I.K.; Sal'nikova, E.B.; Wang, T.; Didenko, A.N.; Plotkina, Y.V.; Podkovyrov, V.N. Early Precambrian Crystalline Complexes of the Central Asian Microcontinent: Age, Sources, Tectonic Position. *Stratigr. Geol. Correl.* **2007**, *15*, 121–140. [[CrossRef](#)]
53. Dijkstra, A.H.; Brouwer, F.M.; Cunningham, W.D.; Buchan, C.; Badarch, G.; Mason, P.R.D. Late Neoproterozoic Proto-Arc Ocean Crust in the Dariv Range, Western Mongolia: A Supra-Subduction Zone End-Member Ophiolite. *J. Geol. Soc.* **2006**, *163*, 363–373. [[CrossRef](#)]
54. Buriánek, D.; Schulmann, K.; Hrdličková, K.; Hanžl, P.; Janoušek, V.; Gerdes, A.; Lexa, O. Geochemical and Geochronological Constraints on Distinct Early-Neoproterozoic and Cambrian Accretionary Events along Southern Margin of the Baydrag Continent in Western Mongolia. *Gondwana Res.* **2017**, *47*, 200–227. [[CrossRef](#)]
55. Skuzovatov, S. Nature and (in-)Coherent Metamorphic Evolution of Subducted Continental Crust in the Neoproterozoic Accretionary Collage of SW Mongolia. *Geosci. Front.* **2021**, *12*, 101097. [[CrossRef](#)]
56. Kröner, A.; Lehmann, J.; Schulmann, K.; Demoux, A.; Lexa, O.; Tomurhuu, D.; Stipska, P.; Liu, D.; Wingate, M.T.D. Lithostratigraphic and Geochronological Constraints on the Evolution of the Central Asian Orogenic Belt in SW Mongolia: Early Paleozoic Rifting Followed by Late Paleozoic Accretion. *Am. J. Sci.* **2010**, *310*, 523–574. [[CrossRef](#)]
57. Lehmann, J.; Schulmann, K.; Lexa, O.; Corsini, M.; Kroner, A.; Stipska, P.; Tomurhuu, D.; Otgonbator, D. Structural Constraints on the Evolution of the Central Asian Orogenic Belt in SW Mongolia. *Am. J. Sci.* **2010**, *310*, 575–628. [[CrossRef](#)]
58. Skuzovatov, S.Y.; Gornova, M.A.; Karimov, A.A. Mineralogical, Geochemical, and Nd-Sr Isotope Characteristics of Amphibolites from the Alag-Khadny High-Pressure Complex (SW Mongolia): Intracontinental Rifting as a Precursor of Continental-Margin Subduction. *Petrology* **2022**, *30*, 523–544. [[CrossRef](#)]
59. Tomurtogoo, O. *Geology of Ophiolitic Complex of Mongolia*; Geological Funds of Mongolia: Ulanbaatar, Mongolia, 1980.
60. Perfiliev, A.S.; Kheraskov, N.N. Diabase Complexes and the Problem of Tectonic Stratification of Oceanic Crust. In *Tectonic Layering of Lithosphere*; Nauka: Moscow, Russia, 1980; Volume 343, pp. 64–104.
61. Hanžl, P.; Aichler, J.; Bolormaa, K.; Budil, P.; Buriánek, D.; Hrdličková, K.; Erban, V.; Gerdes, A.; Gilíková, H.; Holák, J.; et al. *Geological Survey of the Mongolian Altay at a Scale 1:50.000 (Zamtyň Nuruu—50)*; Czech Geological Survey: Prague, Czech Republic, 2007; p. 376.
62. Gornova, M.; Karimov, A.; Skuzovatov, S.; Belyaev, V. From Decompression Melting to Mantle-Wedge Refertilization and Metamorphism: Insights from Peridotites of the Alag Khadny Accretionary Complex (SW Mongolia). *Minerals* **2020**, *10*, 396. [[CrossRef](#)]
63. Skuzovatov, S.Y.; Belozeroва, O.Y.; Vasil'eva, I.E.; Zarubina, O.V.; Kaneva, E.V.; Sokolnikova, Y.V.; Chubarov, V.M.; Shabanova, E.V. Centre of Isotopic and Geochemical Research (IGC SB RAS): Current State of Micro- and Macroanalysis. *Geodin. Tektonofiz.* **2022**, *13*, 0585. [[CrossRef](#)]
64. Amosova, A.A.; Panteeva, S.V.; Tatarinov, V.V.; Chubarov, V.M.; Finkelstein, A.L. X-Ray Fluorescence Determination of Major Rock Forming Elements in Small Samples 50 and 110 Mg. *Anal. Control* **2015**, *19*, 130–138.
65. Rooney, J.S.; Tarling, M.S.; Smith, S.A.F.; Gordon, K.C. Submicron Raman Spectroscopy Mapping of Serpentinite Fault Rocks. *J. Raman Spectrosc.* **2018**, *49*, 279–286. [[CrossRef](#)]
66. Trommsdorff, V.; Evans, B.W. Progressive Metamorphism of Antigorite Schist in the Bergell Tonalite Aureole (Italy). *Am. J. Sci.* **1972**, *272*, 423–437. [[CrossRef](#)]
67. McDonough, W.F.; Sun, S.-s. The Composition of the Earth. *Chem. Geol.* **1995**, *120*, 223–253. [[CrossRef](#)]
68. Kodolányi, J.; Pettke, T.; Spandler, C.; Kamber, B.S.; Gméling, K. Geochemistry of Ocean Floor and Fore-Arc Serpentinites: Constraints on the Ultramafic Input to Subduction Zones. *J. Petrol.* **2012**, *53*, 235–270. [[CrossRef](#)]
69. Brunelli, D.; Seyler, M.; Cipriani, A.; Ottolini, L.; Bonatti, E. Discontinuous Melt Extraction and Weak Refertilization of Mantle Peridotites at the Vema Lithospheric Section (Mid-Atlantic Ridge). *J. Petrol.* **2006**, *47*, 745–771. [[CrossRef](#)]

70. Khedr, M.Z.; Takazawa, E.; Hauzenberger, C.; Tamura, A.; Arai, S.; Stern, R.J.; Morishita, T.; El-Awady, A. Petrogenesis of Arc-Related Serpentinized Peridotites (Egypt): Insights into Neoproterozoic Mantle Evolution beneath the Arabian-Nubian Shield. *J. Asian Earth Sci.* **2022**, *226*, 105078. [[CrossRef](#)]
71. Khedr, M.Z.; Arai, S. Petrology and Geochemistry of Prograde Deserpentinized Peridotites from Happo-O'ne, Japan: Evidence of Element Mobility during Deserpentinization. *J. Asian Earth Sci.* **2012**, *43*, 150–163. [[CrossRef](#)]
72. Kuzmichev, A.B.; Larionov, A.N. Neoproterozoic Island Arcs in East Sayan: Duration of Magmatism (from U–Pb Zircon Dating of Volcanic Clastics). *Russ. Geol. Geophys.* **2013**, *54*, 34–43. [[CrossRef](#)]
73. Takahashi, E.; Uto, K.; Schilling, J.-G. *Primary Magma Compositions and Mg/Fe Ratios of Their Mantle Residues along Mid Atlantic Ridge 29 N to 73 N*; Okayama University: Okayama, Japan, 1987; pp. 1–4.
74. Parkinson, I.J.; Pearce, J.A. Peridotites from the Izu–Bonin–Mariana Forearc (ODP Leg 125): Evidence for Mantle Melting and Melt–Mantle Interaction in a Supra-Subduction Zone Setting. *J. Petrol.* **1998**, *39*, 1577–1618. [[CrossRef](#)]
75. Muntener, O. Cooling History and Exhumation of Lower-Crustal Granulite and Upper Mantle (Malenco, Eastern Central Alps). *J. Petrol.* **2000**, *41*, 175–200. [[CrossRef](#)]
76. Arai, S. Contact Metamorphosed Dunite-Harzburgite Complex in the Chugoku District, Western Japan. *Contr. Mineral. Petrol.* **1975**, *52*, 1–16. [[CrossRef](#)]
77. Evans, B.; Frost, R. Chrome-Spinel in Progressive Metamorphism—A Preliminary Analysis. *Geochim. Cosmochim. Acta* **1975**, *39*, 959–972. [[CrossRef](#)]
78. Trommsdorff, V.; Sánchez-Vizcaíno, V.L.; Gómez-Pugnaire, M.T.; Müntener, O. High Pressure Breakdown of Antigorite to Spinifex-Textured Olivine and Orthopyroxene, SE Spain. *Contrib. Mineral. Petrol.* **1998**, *132*, 139–148. [[CrossRef](#)]
79. Li, X.-P.; Rahn, M.; Bucher, K. Serpentinities of the Zermatt-Saas Ophiolite Complex and Their Texture Evolution. *J. Metamorph. Geol.* **2004**, *22*, 159–177. [[CrossRef](#)]
80. Berman, R.G.; Engi, M.; Greenwood, H.J.; Brown, T.H. Derivation of Internally-Consistent Thermodynamic Data by the Technique of Mathematical Programming: A Review with Application the System MgO-SiO<sub>2</sub>-H<sub>2</sub>O. *J. Petrol.* **1986**, *27*, 1331–1364. [[CrossRef](#)]
81. Berman, R.G. Internally-Consistent Thermodynamic Data for Minerals in the System Na<sub>2</sub>O-K<sub>2</sub>O-CaO-MgO-FeO-Fe<sub>2</sub>O<sub>3</sub>-Al<sub>2</sub>O<sub>3</sub>-SiO<sub>2</sub>-TiO<sub>2</sub>-H<sub>2</sub>O-CO<sub>2</sub>. *J. Petrol.* **1988**, *29*, 445–522. [[CrossRef](#)]
82. Bazylev, B.A. *Petrology and Geochemistry of Oceanic and Alpine-Type Peridotites in Terms of Mantle Evolution Problem*; GEOKHI RAS: Moscow, Russia, 2003; p. 436.
83. Niu, Y. Bulk-Rock Major and Trace Element Compositions of Abyssal Peridotites: Implications for Mantle Melting, Melt Extraction and Post-Melting Processes beneath Mid-Ocean Ridges. *J. Petrol.* **2004**, *45*, 2423–2458. [[CrossRef](#)]
84. Chen, W.; Xiong, X.; Takahashi, E. Zircon Solubility in Solute-Rich Supercritical Fluids and Zr Transfer From Slab to Wedge in the Deep Subduction Process. *JGR Solid Earth* **2021**, *126*, e2021JB021970. [[CrossRef](#)]
85. Louvel, M.; Sanchez-Valle, C.; Malfait, W.J.; Cardon, H.; Testemale, D.; Hazemann, J.-L. Constraints on the Mobilization of Zr in Magmatic-Hydrothermal Processes in Subduction Zones from in Situ Fluid-Melt Partitioning Experiments. *Am. Mineral.* **2014**, *99*, 1616–1625. [[CrossRef](#)]
86. Pens, M.; Andreani, M.; Daniel, I.; Perrillat, J.-P.; Cardon, H. Contrasted Effect of Aluminum on the Serpentinization Rate of Olivine and Orthopyroxene under Hydrothermal Conditions. *Chem. Geol.* **2016**, *441*, 256–264. [[CrossRef](#)]
87. Zheng, Y.-F. Metamorphic Chemical Geodynamics in Continental Subduction Zones. *Chem. Geol.* **2012**, *328*, 5–48. [[CrossRef](#)]
88. Zhang, L.; Sun, W.; Chen, R.-X. Evolution of Serpentinite from Seafloor Hydration to Subduction Zone Metamorphism: Petrology and Geochemistry of Serpentinite from the Ultrahigh Pressure North Qaidam Orogen in Northern Tibet. *Lithos* **2019**, *346–347*, 105158. [[CrossRef](#)]
89. Huang, R.; Lin, C.-T.; Sun, W.; Ding, X.; Zhan, W.; Zhu, J. The Production of Iron Oxide during Peridotite Serpentinization: Influence of Pyroxene. *Geosci. Front.* **2017**, *8*, 1311–1321. [[CrossRef](#)]

**Disclaimer/Publisher's Note:** The statements, opinions and data contained in all publications are solely those of the individual author(s) and contributor(s) and not of MDPI and/or the editor(s). MDPI and/or the editor(s) disclaim responsibility for any injury to people or property resulting from any ideas, methods, instructions or products referred to in the content.